

Performance Studies of $pp \rightarrow pp\pi^0$ and $pp \rightarrow pp\eta$ Reconstruction for the \bar{P} ANDA Day-1 Setup

Master thesis in Physics by Jana Rieger
Date of submission: February 17, 2020

1. Review: Prof. Tetyana Galatyuk
2. Review: Dr. Klaus Götzen
Darmstadt



TECHNISCHE
UNIVERSITÄT
DARMSTADT

Physics Department
Institut für Kernphysik
PANDA, GSI

Erklärung zur Abschlussarbeit gemäß §22 Abs. 7 und §23 Abs. 7 APB der TU Darmstadt

Hiermit versichere ich, Jana Rieger, die vorliegende Masterarbeit ohne Hilfe Dritter und nur mit den angegebenen Quellen und Hilfsmitteln angefertigt zu haben. Alle Stellen, die Quellen entnommen wurden, sind als solche kenntlich gemacht worden. Diese Arbeit hat in gleicher oder ähnlicher Form noch keiner Prüfungsbehörde vorgelegen.

Mir ist bekannt, dass im Fall eines Plagiats (§38 Abs. 2 APB) ein Täuschungsversuch vorliegt, der dazu führt, dass die Arbeit mit 5,0 bewertet und damit ein Prüfungsversuch verbraucht wird. Abschlussarbeiten dürfen nur einmal wiederholt werden.

Bei der abgegebenen Thesis stimmen die schriftliche und die zur Archivierung eingereichte elektronische Fassung gemäß §23 Abs. 7 APB überein.

Bei einer Thesis des Fachbereichs Architektur entspricht die eingereichte elektronische Fassung dem vorgestellten Modell und den vorgelegten Plänen.

Darmstadt, den 17. Februar 2020

J. Rieger

Abstract

The PANDA experiment represents the central part of the hadron physics program at the FAIR facility that is under construction at GSI in Darmstadt. In the early stages of the experiment, during the commissioning phase, a proton beam instead of an antiproton beam will be provided by the accelerator and the reduced Day-1 setup will be available. One of the first experiments that could be performed already during the commissioning phase are cross section measurements of π^0 and η production in proton proton scattering. The reconstruction efficiency for photons, π^0 , η and protons of the Day-1 setup has been studied using PandaRoot simulations. The full production chain including baryonic resonances has been simulated as well and reconstruction efficiencies of the full final state have been determined. There are some losses due to the incomplete Day-1 setup but the relevant phase space for those reactions is covered sufficiently well. PANDA will be able to contribute to the measurement of total as well as differential meson production cross sections with precise measurements.

Contents

1. Introduction	6
1.1. Motivation	7
2. Hadron Physics	8
2.1. The Standard Model of Particle Physics	8
2.2. Hadrons	10
2.2.1. Quantum Chromo Dynamics	10
2.2.2. Static Quark Model	10
2.2.3. Hadronic Resonances	12
2.2.4. Dalitz Plot	13
3. The Experiments	15
3.1. The PANDA Experiment	15
3.1.1. Day-1 Setup	17
3.1.2. Electromagnetic Calorimeter	19
3.1.3. Tracking System	20
4. Software	21
4.1. PandaRoot	21
4.1.1. Simulation	21
4.1.2. Analysis	22
4.2. Pluto	22
5. Particle Reconstruction	24
5.1. Photon Reconstruction	24
5.1.1. Reconstruction Algorithm	24
5.1.2. Simulation	24
5.2. π^0 Reconstruction	29
5.2.1. Merged π^0	30

5.2.2. Simulation	31
5.3. η Reconstruction	32
5.3.1. Simulation	34
5.4. Proton Reconstruction	34
5.4.1. Simulation	34
6. π^0 and η Production in pp Scattering	38
6.1. Simulation	38
6.1.1. π^0 Production	39
6.1.2. η Production	40
6.2. Reconstruction Performance	41
6.2.1. Event Selection	41
6.2.2. Efficiencies	43
6.3. Cross Sections	45
7. Conclusions	50
A. Reconstruction of Merged π^0	52

1. Introduction

Physicists have always tried to find the smallest particles and understand the most fundamental interactions. Hadron physics is one of the field that brings us closer to answering those questions. It deals with the strong interaction, the interaction of quarks and gluons which are the smallest constituents of hadronic matter. Quantum Chromo Dynamics (QCD) is currently the best theory that describes this interaction. Its predictive power at high energies where perturbation theory can be applied, is very good and accepted. Nevertheless, it is difficult to describe processes at low energies, i.e. in the energy regime of hadrons, the bound states of QCD which cannot be predicted perturbatively since the theory becomes strongly coupled in this case. In this non-perturbative regime, it is still hard to make predictions from first principles. In order to shed more light on this physics, we need experiments like \bar{P} ANDA which probe exactly this interesting energy region, [15].

1.1. Motivation

The assembly of the $\bar{\text{P}}\text{ANDA}$ detector is going to be done within the next years. During the Commissioning Phase it will be tested in calibration runs as well as for first physics channels. There will be only a reduced setup available at this stage, the so-called Day-1 setup. While the anti-proton production chain is constructed, the experiment will be provided with a proton beam with luminosities of about $10^{30} \text{ s}^{-1} \text{ cm}^{-2}$ instead of the antiproton beam that will be used in the later runs. This phase is important to test the detector functioning, calibration and performance. At the same time it allows for the production of first physics results [15].

The performance of the detector can be tested by determining the acceptance and detection efficiency for various particle species abundant in final states of hadronic interactions. This information is mandatory to evaluate more complicated reaction channels and to calculate cross sections correctly. In this work the focus is on neutral particles such as gammas, neutral pions and etas. Monte Carlo (MC) studies using the PandaRoot [16] framework and the Pluto [11] event generator are performed to simulate physics reactions and evaluate the detector performance as expected in its early stages.

A physics application directly connected with the reconstruction of neutrals is given by selected meson production cross sections in proton-proton collisions. Interesting channels are $pp \rightarrow pp\pi^0$ and $pp \rightarrow pp\eta$. The study of meson production is important to better understand strong interaction on the hadron level. Especially the production in nucleon-nucleon collisions is of interest since π^0 and η are mainly produced via baryonic resonances. Experimental data can provide quantitative information on hadronic interactions, resonance excitations and their properties. Moreover this information is crucial for the interpretation of heavy ion results. There are some existing measurements of those cross sections by HADES at 1.25 GeV, 2.2 GeV and 3.5 GeV beam kinetic energy [3, 19], measurements from other experiments and theoretical predictions [20] which can be used as benchmarks. It is expected that the $\bar{\text{P}}\text{ANDA}$ experiment is very suitable for cross section measurements of neutral channels due to its solid angle coverage of almost 4π , including the calorimeter and high luminosity. Scans could be performed to measure pp cross sections momentum and angle dependent where no data exists at the moment.

2. Hadron Physics

2.1. The Standard Model of Particle Physics

The standard model describes the established constituents of matter and three of four fundamental forces acting between them. An overview of the particles in the standard model is given in fig. 2.1. There are four groups of particles: leptons, quarks, gauge bosons and the Higgs. Both leptons and quarks are fermions and carry spin $\frac{1}{2}$. The latter two are bosons and have integer spin [12].

Leptons

There are three generations of leptons. The first generation includes the negatively charged electron, the neutral electron neutrino and the corresponding antiparticles. The other two generations are made up in the same way of the μ and τ with their corresponding neutrinos and antiparticles, respectively. The mass is increasing with generation number. All leptons interact by the elektroweak interaction.

Quarks

Quarks carry electrical charge of $\pm\frac{1}{3}$ or $\pm\frac{2}{3}$ as well as color charge. Therefore they are not only affected by the elektroweak interaction but also by the strong interaction. Quarks are always observed in bound states, so-called hadrons. Similar to the leptons the quarks are as well organized in three generations. The first generation is made up of the two lightest quarks, up and down, the other two generations of strange and charm, and beauty and truth, respectively. There are antiquarks corresponding to each quark.

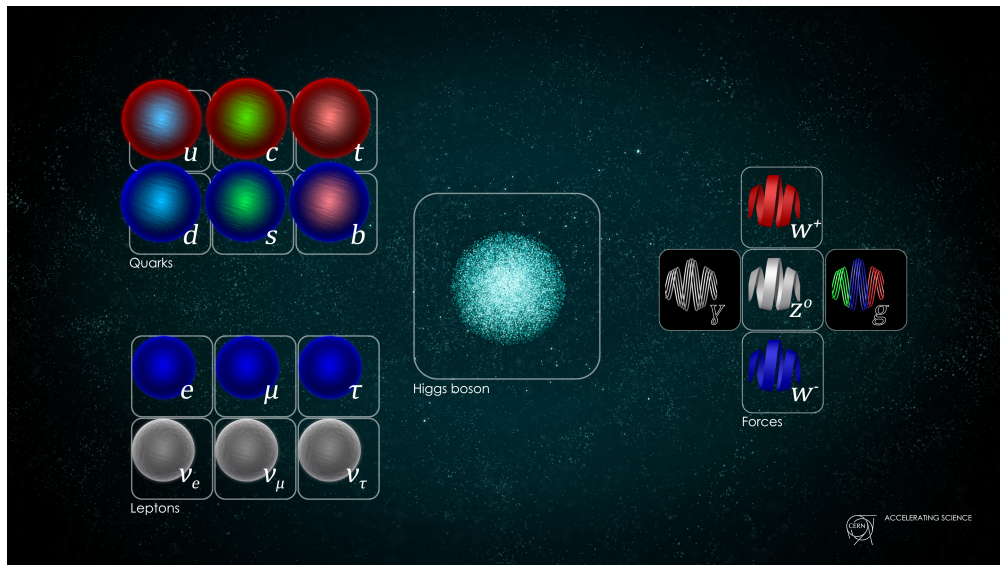


Figure 2.1.: Overview of the particles in the standard model, [18].

Gauge Bosons

The gauge bosons are the mediators of the forces. The electrically neutral photon is the mediator of the electromagnetic interaction. It couples to electrical charge. The W^+ , Z^0 and W^- are the mediators of the weak force. Their masses are about 80 GeV for the W s and 91 GeV for the Z . Due to the uncertainty principle this leads to the short range of the weak interaction. The electromagnetic and weak interaction are theoretically unified to the electroweak interaction. The fourth gauge boson is the gluon. Similar to the photon it is massless and electrically neutral but carries color charge. The gluon is the mediator of the strong force and couples to color charge. It interacts with the quarks and other gluons. The gluon self interaction leads to the theoretical predictions of so-called glueballs, bound states composed only of gluons.

Higgs

The Higgs is the elementary particle with the most recent discovery. It has a mass of about 125 GeV. By spontaneous symmetry breaking of the Higgs field, the mass of the gauge bosons of the weak interaction is created, [13].

2.2. Hadrons

The quarks described in the last section do not exist as free particles but only as the constituents of hadrons, the bound states of QCD.

2.2.1. Quantum Chromo Dynamics

Quantum Chromo Dynamics (QCD) is a field theory that describes the strong interaction. The color charge that the quarks and gluons are carrying is treated similar to the electric charge in QED with the difference that there are three different color charges and not only one. The Lagrangian of QCD is

$$\mathcal{L}_{\text{QCD}} = \bar{\psi}_a (i\gamma^\mu [D_\mu]_{ab} - m) \psi_b - \frac{1}{4} G_{\mu\nu}^\sigma G_{\sigma}^{\mu\nu}, \quad (2.1)$$

where ψ denotes the quark field, γ^μ are Dirac matrices, D_μ the gauge invariant derivative and $G_{\mu\nu}^\sigma$ the gluon field strength tensor.

There are two important principles, that emerge from QCD. One is confinement which means that only color neutral states can be observed. The other is asymptotic freedom. The strong coupling constant becomes weak at high momentum transfers and perturbation theory can be used to calculate those reactions. In the case of small momentum transfers the coupling constant becomes large and this is not possible anymore. This includes the energy regime of hadrons. Lattice QCD can be used to do ab initio calculations here, [13].

2.2.2. Static Quark Model

There are two classes of hadrons: mesons and baryons. One quantity that is conserved in all interactions is the baryon number B . Quarks have $B = \frac{1}{3}$ and antiquarks have $B = -\frac{1}{3}$. Mesons must have $B = 0$. Therefore they consist of the same number of quarks and antiquarks. Baryons have baryon number $B = +1$, antibaryons $B = -1$. Some properties of the hadron spectrum can be predicted by considering symmetries instead of doing the full QCD calculation. If one assumes that the three lightest quarks have the same mass, the light hadrons can be constructed using the SU(3) flavor symmetry. Only the constituent or valence quarks are accounted for here and gluons and sea quarks which are contained in hadrons as well, are omitted. The mesons and baryons that emerge from the static quark model can be arranged in octets and decuplets respectively as suggested by Gell Mann initially [2, 12].

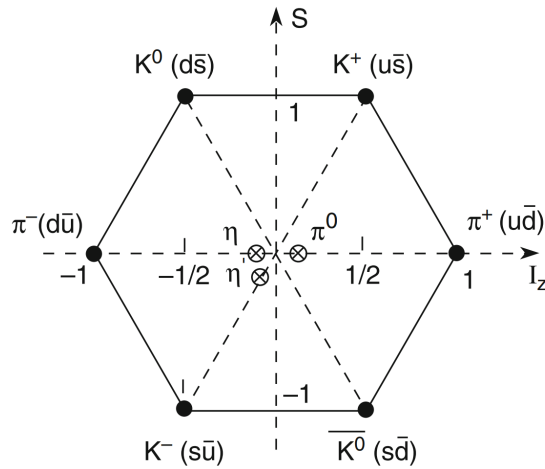


Figure 2.2.: Nonet of mesons with spin parity $J^P = 0^-$ and their quark content., [2].

Pseudoscalar Mesons

The lightest mesons, which have quark content u, d, s , have spin parity $J^P = 0^-$. It is possible to build $3 \times 3 = 9$ quark-antiquark states (a nonet) and arrange them according to their isospin and strangeness as shown in fig. 2.2. The nonet is made of eight states whose wave function is antisymmetric under the exchange of quark flavours (an octet) and a singlet state with a symmetric flavor wave function (the η_1). The mesons are arranged . The π^0 and the η_8 are neutral representatives of the meson octet.

Light Baryons

If we consider the lightest baryons that can be build out of u, d and s quarks with orbital angular momentum 0, we get an octet with spin parity $J^P = \frac{1}{2}^+$ and a decuplet with $J^P = \frac{3}{2}^+$. As for the mesons the baryons of each multiplet can as well be arranged according to their isospin and strangeness as shown in fig. 2.3. The proton is included in the $J^P = \frac{1}{2}^+$ octet, building an isospin doublet with the neutron. The Δ^+ which is an excitation of the proton is included in the Δ quadruplet of the $J^P = \frac{3}{2}^+$ decuplet.

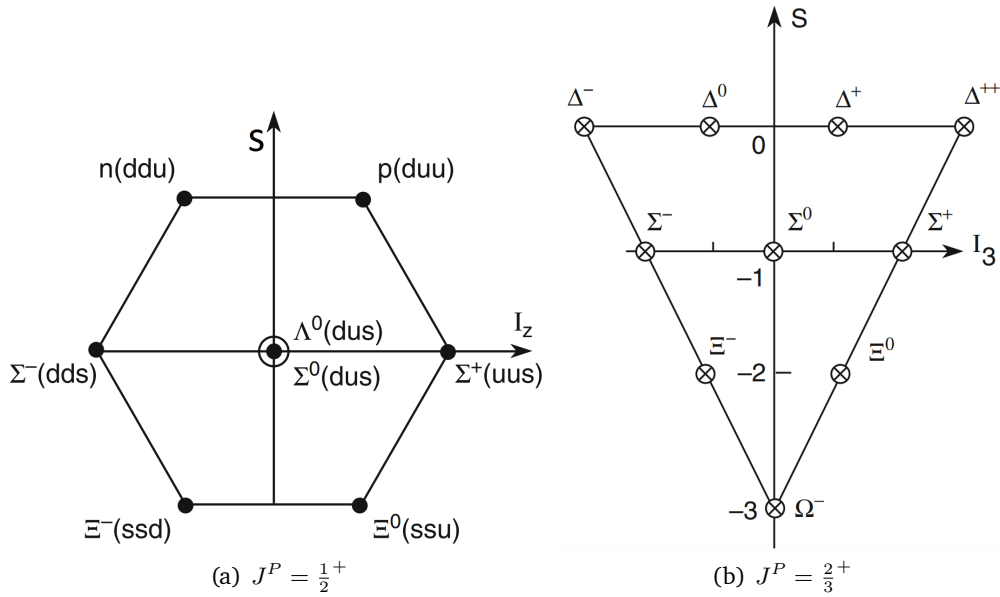


Figure 2.3.: Baryon octet and decuplet, [2].

2.2.3. Hadronic Resonances

If we consider the collision of two hadrons in which the center of mass energy \sqrt{s} and relative angular momentum ℓ of the particles can be varied, it might happen that the cross section passes through a maximum. One can say that there is a hadronic resonance. It is defined by its angular momentum $J = \ell$, parity, isospin, mass $m = E_R = \sqrt{s}$ and lifetime, defined by the width at half maximum Γ of the curve. A resonance implies an increase in the formation probability.

The typical shape of a resonance is shown in fig. 2.4 and is parametrized by

$$\sigma(\sqrt{s}) = \sigma_0 \frac{\Gamma^2/4}{|(E_R - \sqrt{s})^2 + \Gamma^2/4|}, \quad (2.2)$$

called Breit-Wigner. One example of such a resonance is the $\Delta^+(1232)$.

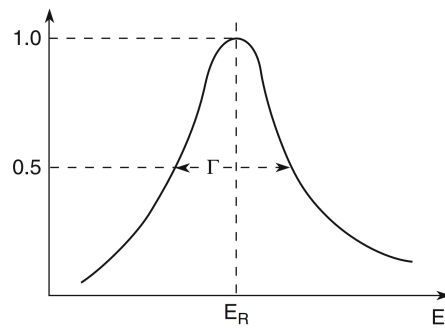


Figure 2.4.: Breit-Wigner shaped resonance [2].

2.2.4. Dalitz Plot

Consider the tree-body decay of a particle with mass M and momentum \mathbf{P} . The masses and momenta of the daughter particles are m_i and \mathbf{p}_i , respectively. Dalitz invented a technique to visualize if the mother particle is decaying via a resonance of two of the daughter particles. Therefore the squares of the invariant mass of two daughters $m_{ij}^2 = (p_i + p_j)^2$ each are plotted against each other. Fig. 2.5 shows such a plot with the kinematical limits that arise from energy conservation. If no resonance is present, the dalitz plot is flat. In case there is a resonance, it appears as a clustering of events along a band at its squared invariant mass in the invariant mass distribution of its daughters.

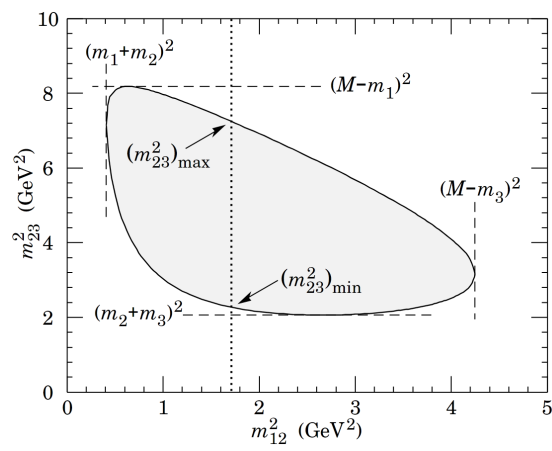


Figure 2.5.: Dalitz plot for a three-body final state. Four momentum conservation restricts events to the shaded region [1].

3. The Experiments

3.1. The $\bar{\text{P}}\text{ANDA}$ Experiment

The $\bar{\text{P}}\text{ANDA}$ Experiment (antiProton ANnihilation at DArmstadt) will be one of the key experiments at the Facility for Antiproton and Ion Research (FAIR) which is currently under construction in Darmstadt, Germany. FAIR is extending the existing heavy ion research center GSI as shown in fig. 3.1. A proton beam will be provided by the existing facility and will be further accelerated by FAIR's SIS100 ring accelerator up to 30 GeV. By the beam hitting the antiproton production target, antiprotons with a momentum of around 3 GeV/ c will be produced and can be collected and pre-cooled in the Collector Ring (CR) and accumulated and decelerated in the RESR (für was auch immer das steht) [17]. Afterwards the antiprotons will be injected into the High Energy Storage Ring (HESR). The race track shaped storage ring (see fig. 3.1) will host the $\bar{\text{P}}\text{ANDA}$ experiment and Koala, a precision scattering experiment for luminosity studies. The antiprotons can be cooled using stochastic and later also electron cooling and afterwards slowed down or further accelerated to momenta from $p = 1.5 \text{ GeV}/c$ up to $p = 15 \text{ GeV}/c$. There are two operation modes of the HESR. In the high-resolution mode a momentum resolution of $\frac{\Delta p}{p} = 5 \cdot 10^{-5}$ and a luminosity of $\mathcal{L} = 1.6 \cdot 10^{31} \text{ cm}^{-2} \text{ s}^{-1}$ can be achieved. In the high luminosity mode the momentum resolution will be $\frac{\Delta p}{p} = 10^{-4}$ and the luminosity $\mathcal{L} = 1.6 \cdot 10^{32} \text{ cm}^{-2} \text{ s}^{-1}$ [HESR, 15].

The $\bar{\text{P}}\text{ANDA}$ detector as shown in fig. 3.3 consists of a Target Spectrometer surrounding the target area and a Forward Spectrometer to detect particles going into the very forward direction. This guarantees an almost 4π acceptance and a good momentum resolution.

There will be various target options. The standard target is a cluster jet target that provides a cluster beam of target gas. Other options are a pellet target consisting of frozen hydrogen pellets or thin foils or noble gases to study antiproton-nucleus interactions.

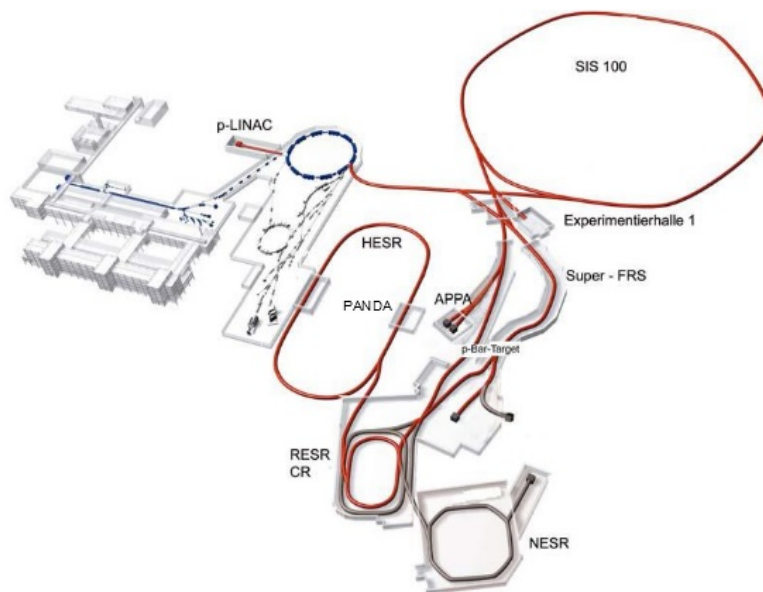


Figure 3.1.: The planned FAIR (red) extending the existing GSI (blue) [TDRTrack].

The Target Spectrometer includes a barrel shaped part as well as a forward and a backward endcap to surround the target almost completely. It is embedded inside a large solenoid magnet, providing a homogeneous magnetic field up to 2T. The interaction point is surrounded by the Micro Vertex Detector (MVD), wrapped by the Straw Tube Tracker (STT) and Gas Electron Multiplier (GEM) stations for tracking of charged particles in the magnetic field. An important feature for particle identification are the DIRC (Detection of Internally Reflected Cherenkov light) detectors. The Electromagnetic Calorimeter (EMC) is used to reconstruct neutral particles and the energy of electrons for particle identification. Furthermore, there is a Time of Flight (ToF) system and muon chambers for particle identification and muon detection.

The Forward Spectrometer covers polar angles below 10° horizontally and 5° vertically. A dipole magnet with variable field strength in combination with several straw tube layers form the Forward Tracking System. Particle identification is provided by the Forward ToF and the Ring Imaging Cherenkov counter (RICH). The EMC is completed by a Shashlyk-type Calorimeter. It is followed by another muon detector, the Muon Range System and the Luminosity Detector at the very end for determination of the interaction rate.

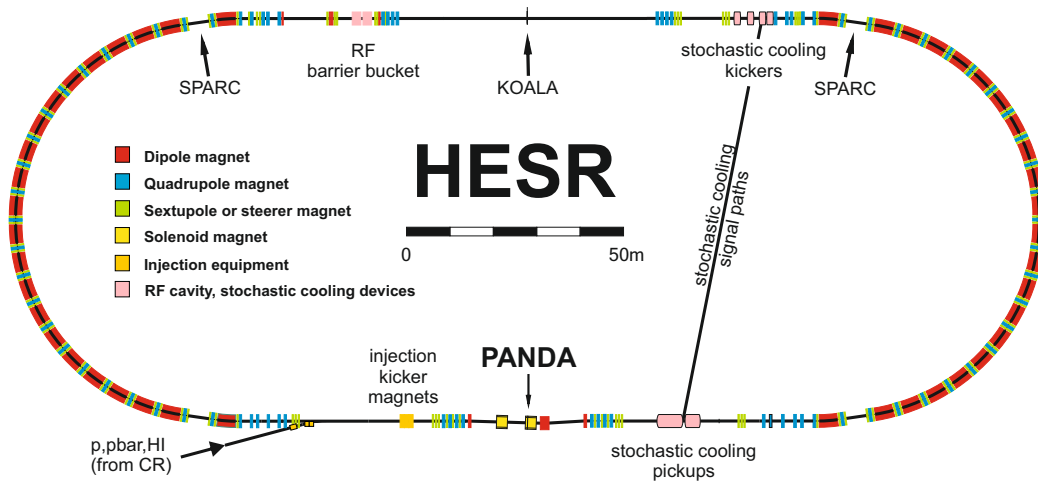


Figure 3.2.: The HESR.

3.1.1. Day-1 Setup

During the first stage of the FAIR project, a reduced setup of the PANDA detector will be available, accounting for available funding, production schedules and the needs of the early physics program [15]. It will be completed and commissioned in 2024. The core systems of the detector such as the cluster-jet target, the solenoid magnet with the muon system, the MVD, the STT, the barrel DIRC and barrel ToF, the forward and backward endcaps of the EMC, 12 slices (out of 16) of the barrel EMC, 2 stations (out of 3) of the GEM detector and 4 (out of 6) stations of the forward tracker, the forward ToF, the forward calorimeter and the luminosity detector are already included in the Day-1 setup. For the forward tracking some existing chambers from LHCb are reused. The missing detector parts to complete the full setup are labeled in red in fig. 3.3.

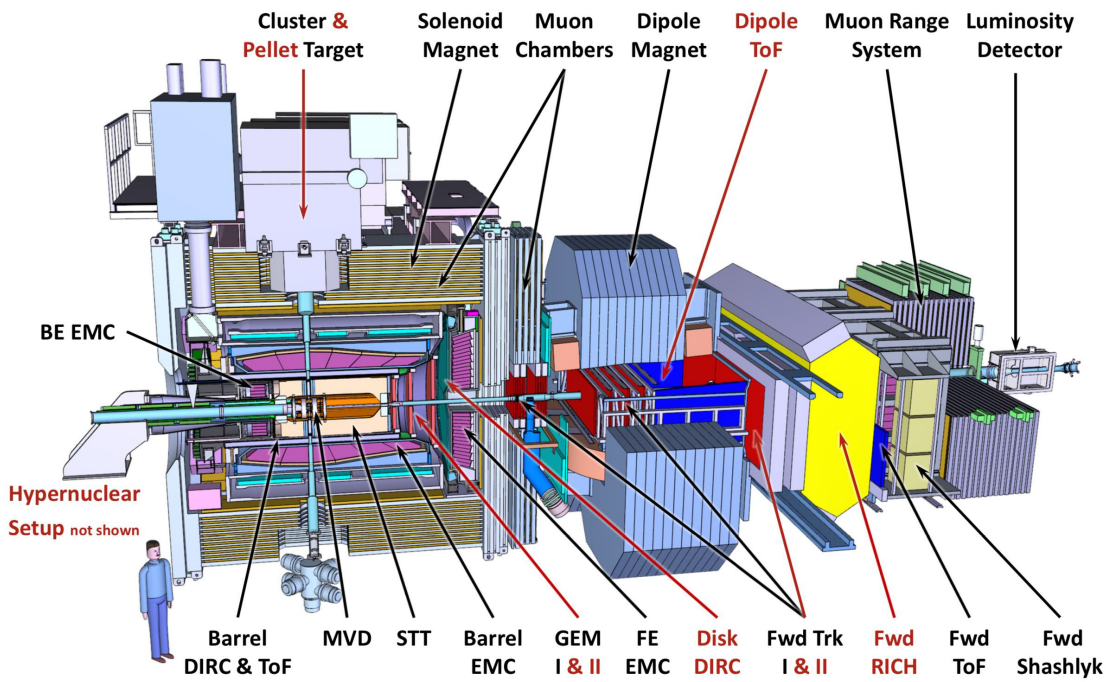


Figure 3.3.: The PANDA detector consisting of Target and Forward Spectrometer. The parts labeled in red are not included in the Day-1 setup [14].

3.1.2. Electromagnetic Calorimeter

In order to detect and measure neutral particles such as photons and π^0 , the ElectroMagnetic Calorimeter (EMC) is the most important subdetector. The PANDA EMC consists of the barrel EMC with the forward and backward endcap EMC in the Target Spectrometer as well as a Shashlyk type EMC in the Forward Spectrometer. It has a 99% coverage of the full solid angle in the center of mass system, making it possible to measure the complete final state, including neutral particles, of many reactions.

The geometry of the Target Spectrometer EMC is summarized in tab. 3.1. It is surrounding the interaction point entirely except for a small gap between the barrel and backward endcap EMC and around the beam pipe. It is an EMC based on scintillator crystals made out of PbWO_4 (PWO). The crystal length corresponds to 22 radiation lengths and the granularity of the detector is chosen related to the Molière radius to guarantee an adequate energy and position resolution [4]. To cover the very forward direction as well, a Shashlyk type EMC is contained in the Forward Spectrometer. It is located at 7.8 m to 8.95 m downstream of the target and consists of 380 layers of lead absorber plates and plastic scintillator tiles corresponding to a total thickness of 19.6 radiation lengths [5].

The energy dependence of the EMC energy resolution for photons is assumed to be of the form

$$\frac{\sigma_E}{E} = a \oplus \frac{b}{\sqrt{E}} \quad (3.1)$$

where E is the energy in GeV and \oplus is the quadratic sum of operands. It is required that $a \leq 1\%$ and $b \leq 2\%$ ($\leq 3\%$ for Forward EMC) and the resolution should be better than 2% for photons above 1 GeV [4, 5]. Furthermore a maximal resolution of 8 MeV is required for reconstructed π^0 .

The barrel EMC is composed of 16 slices - like the planks of a wooden barrel. For the Day-1 setup only 12 of those slices will be completed. That leads to two acceptance holes of 45° in azimuthal direction in the barrel EMC. Therefore a reduced performance is expected in this scenario.

Table 3.1.: Positioning, angular coverage and crystal size of the Target Spectrometer EMC subunits. [4]

EMC Part	Distance to target in z direction	Radius	Angular coverage	Crystal face size
Forward Endcap	2.05 m	0.18 - 0.92 m	5°/10° - 23.6°	24.4x24.4 mm ²
Barrel		0.57 - 0.94 m	22° - 140°	21.3x21.3 mm ²
Backward Endcap	-0.55 m	0.1 - 0.3 m	151.4° - 169.7°	20.5x20.5 mm ²

3.1.3. Tracking System

In order to measure reactions like $pp \rightarrow pp\pi^0$ or $pp \rightarrow pp\eta$ exclusively, it is necessary to reconstruct the full final state. The neutral particle can be reconstructed from the signal of the two photons it is decaying to, detected in the EMC. For the reconstruction of charged particles a tracking system is needed. In PANDA it will consist of four subsystems drawn in red in fig. 3.3.

The Micro-Vertex-Detector (MVD) is the innermost part of the Target Spectrometer, directly surrounding the primary interaction point. It is made out of several detector layers confined in a cylinder with a radius of only 15cm. It covers polar angles from 3° up to 150°. The layers are a mix of silicon hybrid pixel sensors for the inner layers and double sided silicon strip detectors building the outer layers [6].

The central tracker of the Target Spectrometer will be realised as a Straw Tube Tracker (STT). It consists of multiple layers of tubes filled with gas and a wire, basically single channel drift tubes. When a charged particle traverses such a tube, it can ionize the gas and an electric signal can be measured after charge separation due to a high voltage that is applied between the tube and the wire. The STT with an outer radius of 45 cm surrounds the MVD and covers a polar angle range from about 10° to 140° [10].

A set of large area planar Gaseous Electron Multipliers (GEM) detectors is following the STT in forward direction covering polar angles from 3° to 20°.

Furthermore the Forward Spectrometer contains a Forward Tracker that includes six tracking stations made out of straw tubes like the STT. It is designed for momentum analysis of charged particles. The stations are placed directly in front of, inside and behind the dipole magnet. The Forward Tracker is covering polar angles up to $\pm 10^\circ$ horizontally and $\pm 5^\circ$ vertically [7].

4. Software

4.1. PandaRoot

The PandaRoot software framework [Spataro_2012] is the software that was mainly used to obtain the results presented in this thesis. It is the off-line software for the PANDA detector simulation and event reconstruction. Since it is still under development, there are new releases which bring big improvements regularly. The release that is used here is the October 2019 release.

PandaRoot is implemented inside the FairRoot [FairRoot] framework which is used by all big FAIR experiments. FairRoot is based on the ROOT [Brun:1997pa] package and handles basic features such as the interfaces to simulation, geometry handling, parameter database and I/O. It allows for different microscopic particle transport models such as GEANT3 and Geant4. The specifics of the PANDA detector and the reconstruction code are implemented inside PandaRoot.

The PandaRoot framework will be used for Monte Carlo studies as well as for the analysis of data that is taken in the future. In doing so there will be a good comparability of results obtained by simulated and real data analysis.

4.1.1. Simulation

In order to get a good estimate of the detector performance and reconstruction efficiency of specific channels, it is necessary to simulate large amounts of events to reduce statistical fluctuations. The first simulation step is the event generation. There are several event generators available, which are used to investigate various scenarios of interest. EvtGen is an event generator that was used by many B-physics experiments and is now included in PandaRoot. It is used here to simulate events with phase space distributed decay particles. If it is required to simulate data including resonances in the decay products,

other generators can be used to provide an input to PandaRoot. The Pluto event generator (see sec. 4.2) is used here to simulate meson production in pp scattering via a baryonic resonance. Moreover there is a box generator. It allows the simulation of particles of arbitrary species, multiplicity, momentum and direction. This generator is used to map out the detector acceptance of the relevant final state particles γ , π^0 , η and p . After event generation the generated particles are decayed (in case of unstable particles) and propagated through the detector by the selected transport model software package. The default, GEANT3, is used in this work. Charged tracks are reconstructed combining the hits from the different tracking detectors and extrapolating them to PID (particle identification) detectors. Provided that information charged candidates are formed. The PandaRoot framework offers various options for the track finding and reconstruction algorithms. The ones that are used in this work are "multikalman proton" which activates kalman filtering with the proton hypothesis, and "barreltrack" which does not require hits in the STT and provides a more realistic tracking. If there is a cluster in the EMC that is not associated with a charged track, a neutral candidate (i.e. a photon) is formed based on the observed energy deposit. The output of the simulation are two ROOT files, one with the simulation data and one with the PID information.

4.1.2. Analysis

After the detector response to the generated particles has been simulated, the so obtained Monte Carlo data can be analyzed with the same tools that will be used for real data analysis. The user has the possibility to use a predefined analysis macro or to fill candidate lists himself. PID selections and kinematic constraints can be applied here as well as different kinematic and vertex fitters that constrain the four vectors of the entire decay tree. The associated generator information (so-called Monte Carlo Truth) can be retrieved to be compared with the reconstructed data.

4.2. Pluto

The Pluto event generator [11] was originally developed for the HADES experiment. It is a Monte-Carlo event generator designed for hadronic interactions from the pion production threshold up to energies of a few GeV per nucleon and for studies of heavy ion reactions. The package is based on ROOT and uses the embedded C++ interpreter. Pluto was used here to simulate baryonic resonances in π^0 and η production. One million events can be

generated within a few minutes. The output is a ROOT or ASCII file and can be used as input in PandaRoot to simulate the detector response.

Resonance production is performed with mass-dependent Breit-Wigner sampling and the widths of unstable particles are calculated recursively with a coupled-channel approach.

5. Particle Reconstruction

5.1. Photon Reconstruction

Photons are one of the most abundant particles that will be produced in reactions at the $\bar{\text{P}}\text{ANDA}$ experiment and are the most prominent decay product of π^0 and η which are investigated later. They will cover a wide energy range from a few MeV up to 15 GeV. The essential subdetector for photon reconstruction is the EMC.

5.1.1. Reconstruction Algorithm

If a photon is entering one scintillator module, it is producing an electromagnetic shower that is in general extending over several modules. A digi is the digitized signal information from a module in PandaRoot. A cluster is build by a set of digis, including their spatial alignment information, that are representations of excited modules of the EMC in a contiguous area. The four vector of the initial photon can be reconstructed by considering the energy deposit and shape of a cluster, and assuming a certain space coordinate as origin (e.g. the interaction point). After all adjacent digis that exceed a certain energy threshold are added to the cluster, a bump splitting algorithm is run that searches for local maxima within the cluster. Such maxima can occur if the cluster was produced by more than one particle. If a local maximum is found, the cluster is split into bumps associated with a neutral particle candidate. Therefore the digis of the cluster are assigned to the bumps with weights calculated by an iterative procedure.

5.1.2. Simulation

In order to test the photon reconstruction performance of the $\bar{\text{P}}\text{ANDA}$ detector as it is implemented in PandaRoot, a set of single photon events is generated. Three directions

at $\varphi = 27circ$ and $\vartheta = 3^\circ, 15^\circ$ and 57° , corresponding to the forward shashlik, forward endcap and barrel EMC respectively, are chosen. A box generator is used to generate single photons at energies varying from 0.03 to 12 GeV going in those specific directions. 2000 simulated events for each energy and direction setting are sufficient to provide good suppression of statistical effects. The events are simulated using PandaRoot [16] simulation and analyzed afterwards.

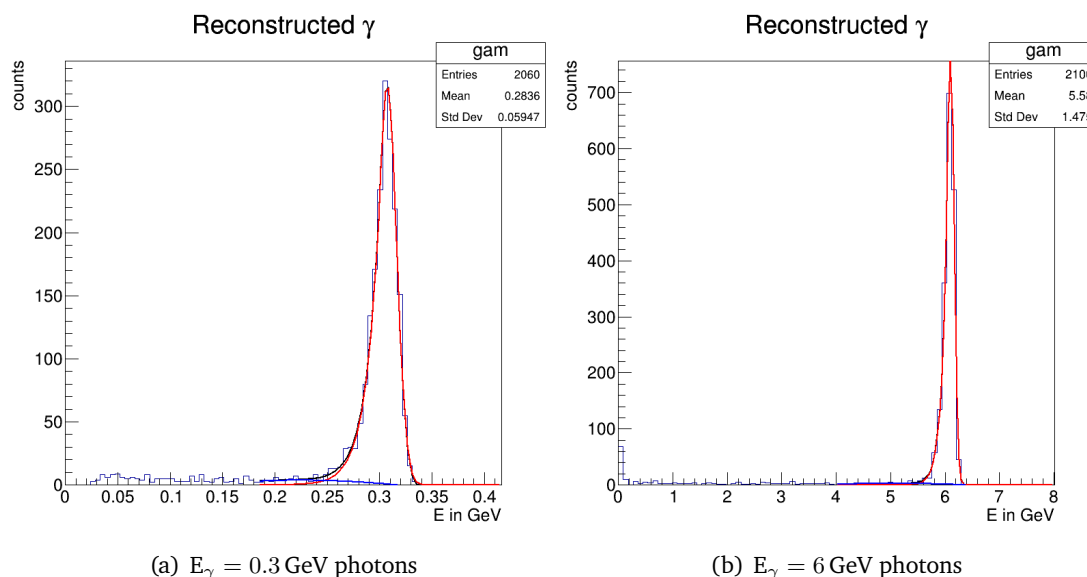


Figure 5.1.: Example reconstructed photon energy spectra from 2000 generated photons with fit of function (5.1). The signal function is shown in red, the background in blue.

Examples of the resulting photon energy spectra are displayed in fig. 5.1. One can see a distribution of photon energies that peaks at about the generated energy. There is a very flat distribution of photons that have a lower energy than the generated one. Those result from interaction of the primary photons with the detector material. An energy threshold of 25 MeV has been set for EMC clusters to be considered as particle candidates to avoid the background at very low energies. The main photon peak has a tail at the left side that is resulting from energy loss due to interaction of photons with detector material. Function (5.1) combined with a second order polynomial as background is fitted to the photon peak. It parametrizes a gaussian distribution with an additional tail on the left

side.

$$f(x) = \begin{cases} A \cdot \exp \left[-\frac{1}{2} \left(\frac{x-\mu}{\sigma} \right)^2 \right] & \text{for } \frac{\mu-x}{k \cdot \sigma} \leq 1 \\ A \cdot \exp \left[-\frac{1}{2} k^2 + k \cdot \left(\frac{x-\mu}{\sigma} \right)^2 \right] & \text{for } \frac{\mu-x}{k \cdot \sigma} > 1 \end{cases} \quad (5.1)$$

A is the magnitude parameter, μ the mean, σ the width of the distribution, and k describes the tail. The function describes the photon peak well. The integral of the fitted function without background represents the number of reconstructed photons. After dividing this number by the number of generated events, the reconstruction efficiency is obtained. It is shown for the different EMC subdetectors in fig. 5.2. For barrel and forward endcap the efficiency varies between 75% and 95% and is slightly better for the barrel EMC. The photon reconstruction efficiency of the Shashlyk Forward EMC is significantly lower at only around 70% and has a larger spread which is due to a worse resolution and fit uncertainties. The insufficient performance of the Shashlyk EMC is expected since its simulation in PandaRoot is not completed yet. The solid errorbars indicate the statistic error, the outer ones the total error. The systematic error is determined by varying the fit range. The weighted average of the efficiency ϵ is calculated for each part using (5.2).

$$\hat{\mu} = \frac{1}{w} \sum_{i=1}^n w_i \epsilon_i \quad (5.2)$$

with $w_i = 1/\Delta\epsilon_i$ and $w = \sum_i w_i$ [1]. The standard deviation of $\hat{\mu}$ is $1/\sqrt{w}$. This results in $\epsilon_{\text{Brl}} = (90.3 \pm 2.6)\%$ for the barrel EMC, $\epsilon_{\text{FWE}} = (85.2 \pm 1.5)\%$ for the forward endcap and $\epsilon_{\text{Shs}} = (66.0 \pm 2.6)\%$ for the Shashlyk EMC.

Fig. 5.3 shows the energy resolution of the reconstructed photon peak, quantified by the σ of the gaussian part of the signal function as obtained from the fit, divided by the photon energy. An empirical resolution function (3.1) that is given in the TDR, is fitted to the points. The results and the requirements from the TDRs are listed in tab. 5.1. The function describes the photon resolution well in case of the Target Spectrometer and the fitted parameters fulfill the requirements from the TDR [4]. Furthermore, the single photon resolution is better than 2% for photons above 1 GeV which is required as well. Concerning the Forward (Shashlyk) EMC, larger fluctuations and errors are found and the fit of function (3.1) describes the points not as well. The photon resolution is worse than required in the TDR [5]. This part of the EMC, as it is currently simulated in PandaRoot,

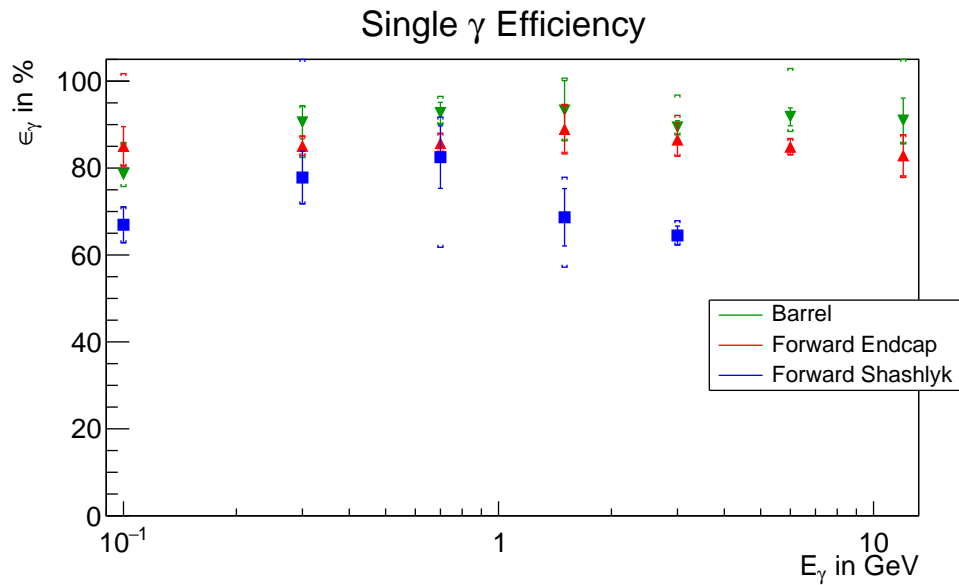


Figure 5.2.: Single photon reconstruction efficiencies for photons generated in specific spatial directions corresponding to each EMC part. The statistical errors (colored) result from the fit and the calculation of the integral, the total error including systematics is also shown.

does not meet the requirements.

Shashlyk EMC

The implementation of the Shashlyk EMC in PandaRoot is not yet completed. That could be the reason for the insufficient performance that simulations show for this EMC subdetector at the moment. Taking a look at the spectrum in fig. 5.4 reveals a possible deficiency of the bump splitting algorithm at higher energies. The peaks at 5.4 GeV and 0.6 GeV suggest that some of the photons are producing clusters that are so large that they get split by the bump splitting algorithm although they belong to one photon hit. This makes it hard to reconstruct the initial photon and the data points at 6 GeV and 12 GeV had to be excluded from the above analysis.

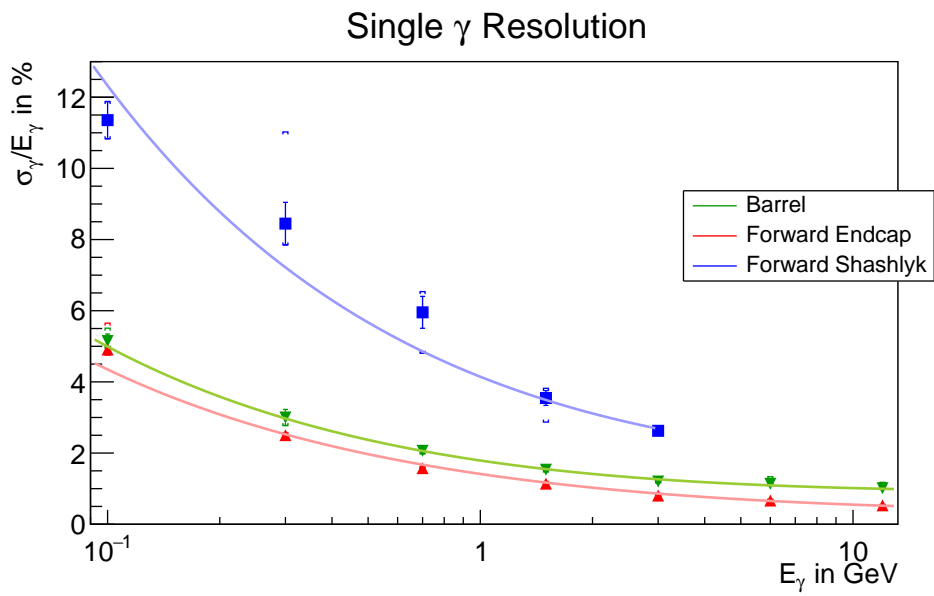


Figure 5.3.: Single photon resolution (σ of gaussian part of signal function) for photons generated in specific spatial directions corresponding to each EMC part.

Table 5.1.: Photon energy resolution fit parameters (eq. 3.1) for the three subdetectors. The TDR requirements are listed in brackets.

EMC Part	a in %	b in %
Forward Endcap	0.89 ± 0.04 (≤ 1)	1.55 ± 0.05 (≤ 2)
Barrel	0.34 ± 0.03 (≤ 1)	1.37 ± 0.02 (≤ 2)
Forward (Shashlyk)	1.49 ± 0.26 (≤ 1)	3.87 ± 0.15 (≤ 3)

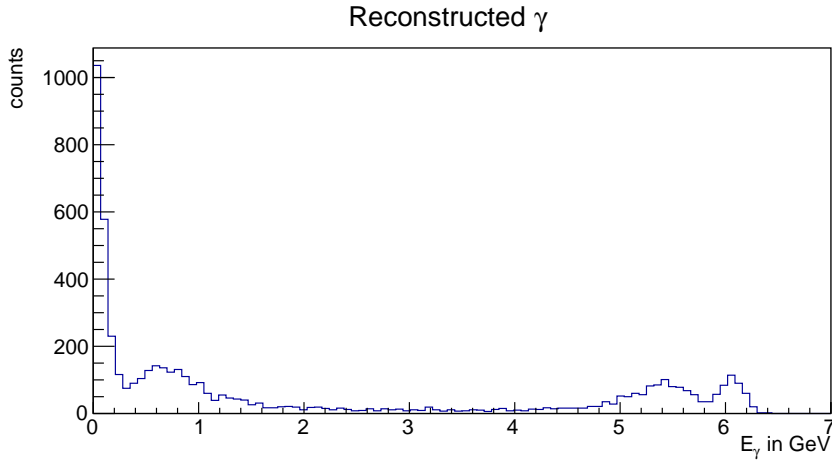


Figure 5.4.: Example reconstructed photon energy spectra from 2000 generated photons at 6 GeV in the Shashlyk EMC.

5.2. π^0 Reconstruction

The π^0 is the lightest meson. Since it is often among the recoiling particles or decay products of interesting hadronic resonances but also part of the hadronic background, it is important to know the detector response and detection efficiency for π^0 as precisely as possible. The π^0 is composed of two light quarks

$$|\pi^0\rangle = \frac{1}{\sqrt{2}} |u\bar{u}\rangle - \frac{1}{\sqrt{2}} |d\bar{d}\rangle. \quad (5.3)$$

It has a rest mass of $m_{\text{PDG}} = 134.9766$ MeV and a mean life of $\tau = 8.52 \cdot 10^{-17}$ s, decaying into two photons with a branching ratio of 98.823% [1].

Due to its short lifetime the π^0 is decaying almost at its point of creation. It can be

reconstructed by combining the four-vectors of its daughter photons. In order to find the right photons in the large amount of photon candidates produced in one event, all possible pairs of two photon candidates are combined. By looking at the invariant mass spectrum of the photon pairs found in a large number of events, the π^0 can be identified as a resonant structure that is peaking around the π^0 mass. The π^0 yield can be extracted from this spectrum by fitting a suitable function to it. Usually a gaussian-shaped signal function and a low order polynomial as background is combined. The integral of the signal function gives the particle yield.

Since no particle detector is perfect, there will always be losses. If one of the daughter photon is not found, the π^0 cannot be reconstructed. One reason for such losses are acceptance holes in the detector coverage. If a photon is emitted in the direction of the missing EMC slices or hits the support frame instead of active detector, it is lost. Moreover the reconstruction algorithm is imperfect which can result in a charged particle's energy deposit in the EMC being identified as a photon or a π^0 might be identified as background.

5.2.1. Merged π^0

In the π^0 rest frame the daughter photons are emitted back to back to satisfy momentum conservation. In the laboratory frame the photons are Lorentz boosted in the direction of the π^0 momentum. If the momentum of the π^0 is large, it might happen that the photons are emitted with a very small opening angle. If this angle becomes so small that they hit the same or directly neighboring EMC crystals, they cannot be resolved as two photons anymore. Since the signals of the individual photons merge to a single cluster, this incident is called "merged π^0 ". The minimum opening angle at which the photons from π^0 decay can be emitted in the laboratory frame due to the Lorentz boost, is realized if the photons are emitted at $\theta = 90^\circ$ with respect to the momentum vector of the π^0 in its rest frame. It can be expressed as

$$\theta'_{\min} = 2 \cdot \arctan\left(\frac{m_{\pi^0} c}{p'_{\pi^0}}\right) \quad (5.4)$$

in the laboratory frame. p_{π^0} is the magnitude of the pion momentum in the laboratory frame. This angle can be converted to minimal hit distance on the EMC surface by

$$d_{\min} = 2r \tan \theta'_{\min} \approx 2r \theta'_{\min} \quad (5.5)$$

for small opening angles. r is the distance from the interaction point to the EMC surface. Fig. 5.5 shows the minimal hit distance of the daughter photon from π^0 decay on the EMC

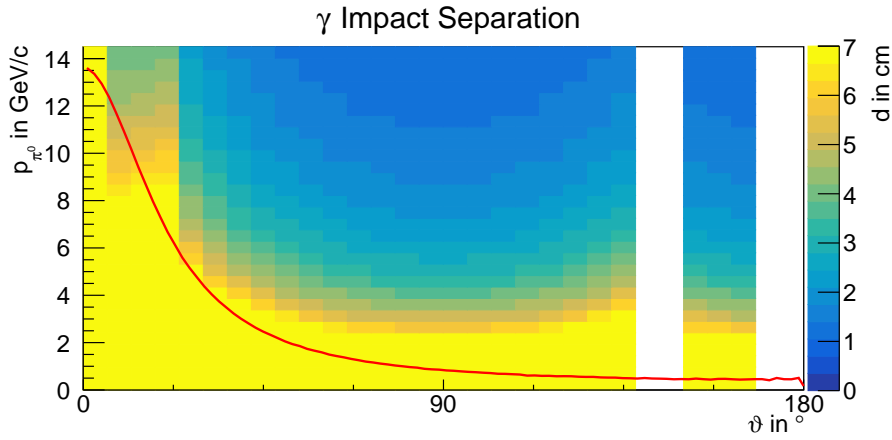


Figure 5.5.: Hit distance in cm on the EMC surface of the daughter photons from π^0 decay. The red line indicates the upper bound of the available kinematic phase space for $pp \rightarrow pp\pi^0$ production at $p_{\text{beam}} = 15 \text{ GeV}/c$.

surface depending on the pion momentum and polar angle as well as the available kinematic phase space if a proton beam of $15 \text{ GeV}/c$ is used. The maximum photon separation at which merging of the π^0 would occur is 6 cm if two diagonally adjacent crystals are hit. One can see that the separation will be larger in this scenario and that merging is not expected.

In case merged π^0 are occurring in another scenario, they can be resolved using the moments analysis of EMC clusters. By calculating the invariant mass of the cluster, it can be decided whether the hit was produced by a merged π^0 or a single photon. This procedure is described in A.

5.2.2. Simulation

In order to test the detector acceptance and detection efficiency of π^0 , one million isotropically distributed box generator π^0 events were generated, across a momentum range between $0.05 \text{ GeV}/c$ and $5 \text{ GeV}/c$. Those π^0 are decayed and transported through the detector by GEANT3 and the detector response is simulated by PandaRoo using the Day-1 setup.

The analysis of the pions from the reconstructed data is performed in the same way

as described above, using a 200 MeV window around the nominal π^0 mass to reduce combinatorics.

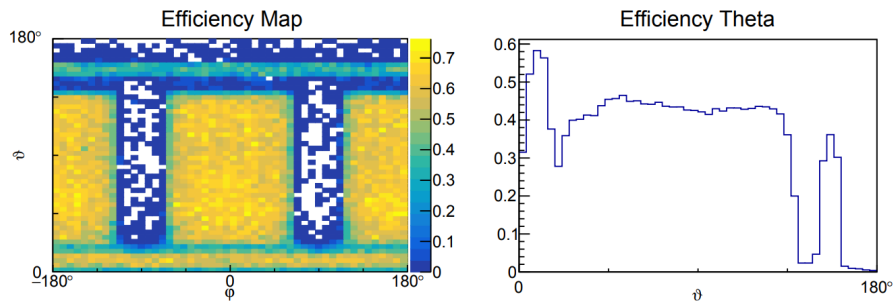
An efficiency map is produced by segmentating the phase space into 50 slices in momentum (p) or azimuthal (φ) and polar (ϑ) direction, resulting in a two dimensional map as shown in fig. 5.6. The π^0 yield is extracted for each individual bin from the invariant mass spectrum by fitting function 5.1 to it and calculating the yield. Afterwards this number is divided by the number of π^0 that were generated in that bin corrected by the branching ratio $\text{BR}(\pi^0 \rightarrow \gamma\gamma) = 98.823\%$ [1]. The result is the π^0 reconstruction efficiency of the corresponding phase space location. The maps are shown in fig. 5.6. The detector structure is visible very good in the $\vartheta - \varphi$ map. One can clearly see the regions that are covered by the EMC where the efficiency is high. There are only very few reconstructed events in the direction of the missing EMC slices, in the very backward direction and in the overlap region of the barrel and forward endcap EMC. The large opening angle of the daughter photons at low pion momentum makes it possible to reconstruct some π^0 events in directions, not covered by the EMC. Looking at the $p - \vartheta$ map, the efficiency is almost isotropic at low momenta due to averaging because of the large photon opening angle. At higher pion momenta, when the daughter photons hit the same subdetector, the detector structure becomes visible. One can see an acceptance drop at the highest pion momenta in the barrel which is due to merging of the π^0 . A projection of the maps on the pion's momentum and polar angle respectively is shown as well. The overall efficiency is at almost 40%, averaging over the entire detector. In the regions that are covered by the EMC, the efficiency is between 60% and 70%.

5.3. η Reconstruction

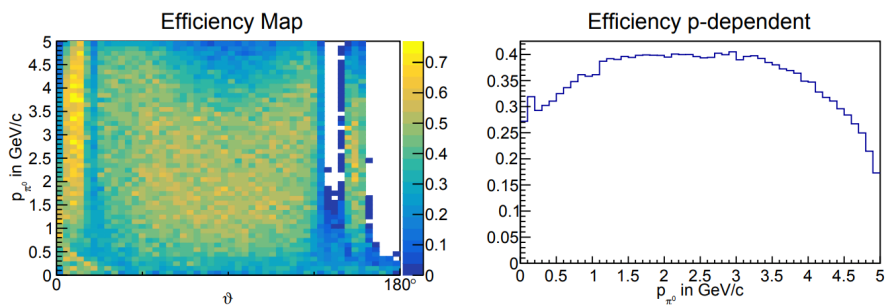
The η is the next heavier neutral meson after the π^0 and can therefore be found in many hadronic interactions as well. It is composed of two quarks but in contrast to the π^0 it has some strangeness contribution. It is a linear combination of the singlet state η_1 and the octet state η_8 with a mixing angle of $\theta \approx 11^\circ$ [2]. Their wave functions are

$$|\eta_1\rangle = \frac{1}{\sqrt{3}} (|u\bar{u}\rangle + |d\bar{d}\rangle + |s\bar{s}\rangle) \quad \text{and} \quad |\eta_8\rangle = \frac{1}{\sqrt{6}} (ketu\bar{u} + |d\bar{d}\rangle - 2|s\bar{s}\rangle). \quad (5.6)$$

The η has a rest mass of $m_{\text{PDG}} = 547.862 \text{ MeV}$ and a width of $\Gamma = 1.31 \text{ keV}$. The dominant decay modes are $BR = \eta \rightarrow \gamma\gamma$ with a branching ratio of $\text{BR} = 39.41\%$, $\eta \rightarrow 3\pi^0$ with $\text{BR} = 32.68\%$ and the charged mode $\eta \rightarrow \pi^+\pi^-\pi^0$ with a branching ratio of $\text{BR} = 22.92\%$ [1]. Since the electromagnetic decay is the only one that is considered here, the



(a) Left: ϑ - φ map, right: Projection onto ϑ . The first spike corresponds to the Forward EMC, the plateau to the barrel part and the small spike to the backward endcap.



(b) Left: p - ϑ map, right: Projection onto p .

Figure 5.6.: Efficiency maps for isotropically distributed π^0 with momenta between 0.05 GeV/c and 5 GeV/c. .

reconstruction is performed in the same way as for the π^0 . Due to the larger mass and thus larger opening angle it is not expected that merged η are occurring in the relevant momentum range.

5.3.1. Simulation

The test of the detector acceptance and detection efficiency of η is done in the same way as for the π^0 . Since the η has a worse reconstructed mass resolution, a mass window of 500 MeV around the nominal η mass is chosen and 2.5 million events were generated to account for the lower branching ratio of the electromagnetic decay.

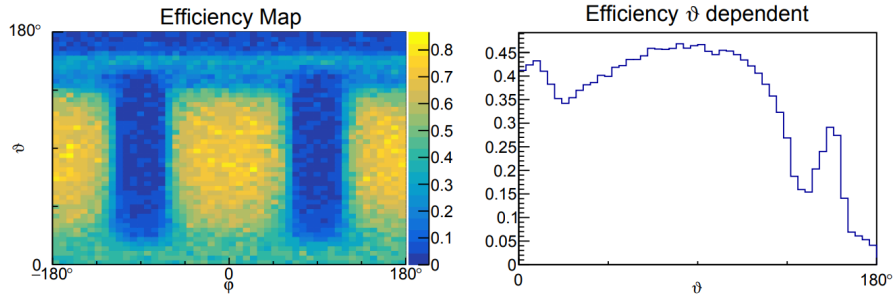
The reconstruction efficiency for η (see fig. 5.7) is similar as in the π^0 case. The detector structure is less visible. This is because of the larger mass of the η and the consequentially larger opening angle of the daughter photons. This results also in a lower efficiency in forward direction, especially at low momenta, since some of the photons are going into the region with low performance at the overlap of barrel and forward endcap EMC. The efficiency in the active part of the barrel EMC is very good with around 70%. As expected the $p - \theta$ map does not show any hints of merged η at large momenta in the barrel region. The efficiency is isotropic up to $p = 1.5$ GeV and dependent on the detector structure at higher momenta. If averaging over the full solid angle, the efficiency seems independent of p . The averaged reconstruction efficiency of the entire detector is almost 40%.

5.4. Proton Reconstruction

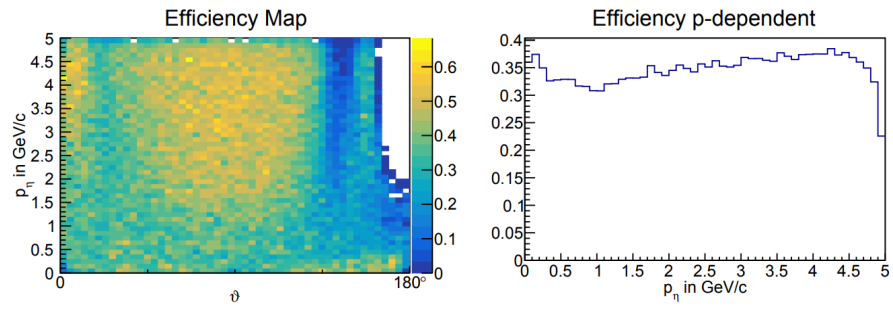
During the first time of \bar{P} ANDA data taking a proton beam on a hydrogen target will be used. If the full final state of proton scattering events is to be reconstructed, it is necessary to detect the scattered beam and target proton. As for other charged particle species, several tracking and PID detectors are relevant here.

5.4.1. Simulation

To probe the proton acceptance of the detector, 500 000 single proton events that are distributed isotropically with a momentum range from 0.05 GeV/ c to 5 GeV/ c have been generated using the box generator and processed through the detector and reconstructed



(a) Left: ϑ - φ map, right: Projected ϑ distribution.



(b) Left: p - ϑ map, right: Projected p distribution.

Figure 5.7.: Efficiency maps for isotropically distributed η generated at momenta between $0.05 \text{ GeV}/c$ and $5 \text{ GeV}/c$. (a) The first dip in the projected ϑ distribution corresponds to the overlap region of barrel and forward endcap EMC, the small spike at 160° to the backward endcap.

in PandaRoot. The fraction of reconstructed protons reflects the detector acceptance.

The requirements for a proton to be reconstructed are either a minimum of four hits in the Micro Vertex Detector or at least six hits in a tracking detector (MVD, STT and GEM hits combined) charge +1 assigned to the charged candidate associated with the track. The proton tracks that fulfill this requirement are shown in fig. 5.8 where the bins are assigned according to the initial momentum direction of the protons. The proton acceptance is around 80% for most parts of the phase space. There are no accepted protons in the backward direction for $\vartheta > 110^\circ$ due to the few tracking detectors in that region which leads to too few hits for track reconstruction. This barely restricts the detector performance since most particles get a strong forward boost in fixed target experiments. Small acceptance holes can also be found at $\varphi = \pm 90^\circ$ where the target pipe and support structures are located. Those holes are not relevant due to the symmetry in φ of the interactions. The $\vartheta - \varphi$ map is divided into six slices, corresponding to the six submodules of the STT. More relevant acceptance holes can be found for $p < 0.2$ GeV where the protons are too slow to emerge the beam pipe and for $\vartheta < 4.4^\circ$. Here are not enough tracking stations to get enough hits and the beam pipe restricts the detector coverage at very small polar angles. In the full \bar{P} ANDA setup there will be two more tracking stations in the forward spectrometer which might improve the performance here. The performance of detecting protons gets worse at large particle momentum. Charged particles are less deflected by the magnetic field at large momentum which makes it less likely to produce enough hits in the detector. In contrast the performance is very good at low proton momentum.

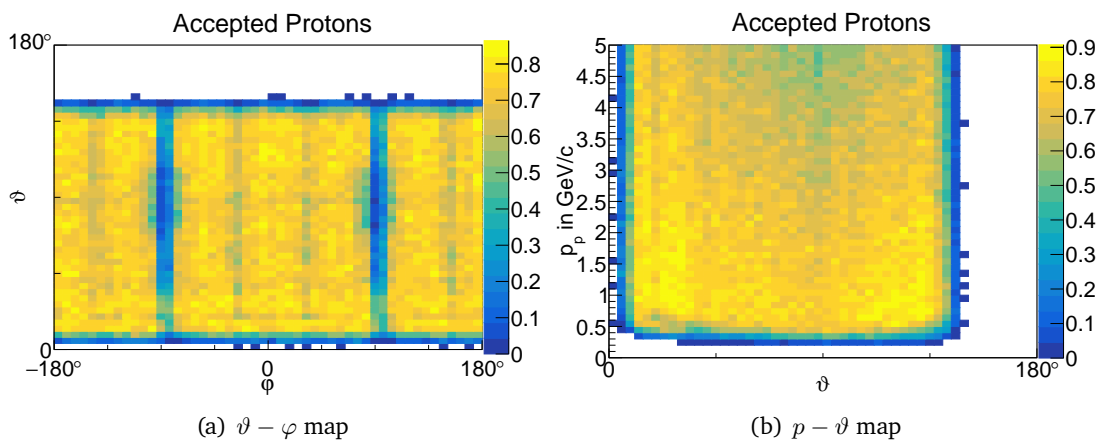


Figure 5.8.: Acceptance maps of the $\bar{\text{P}}\text{ANDA}$ detector for single protons.

6. π^0 and η Production in pp Scattering

The determination of meson production cross sections in pp scattering are measurements that can already be performed during the commissioning phase of \bar{P} ANDA. Since the beam will have a very good momentum resolution and the \bar{P} ANDA detector a very good coverage of the full solid angle, it will be possible to measure integrated and differential cross sections for beam momenta up to 15 GeV/ c . Especially for high energies there exist no precise measurements of differential cross sections yet. There are measurements of π^0 and η production by HADES at 1.25, 2.2 and 3.5 GeV kinetic beam energy [3, 19]. This data is used to compare with the simulations for \bar{P} ANDA .

6.1. Simulation

In order to test the performance of the \bar{P} ANDA detector to measure the relevant cross sections, several Monte Carlo datasets have been generated, covering the full accessible energy range. Both, production with an isotropic phase space distribution using the EvtGen event generator as well as resonant production with a selected baryonic resonance, are tested. In the latter case the reaction is simulated using the Pluto event generator with the same model that was used in the HADES analysis [3, 19].

After the event generation the particles are processed through the \bar{P} ANDA detector with PandaRoot. For particle reconstruction the tracking options "barreltrack" and "mulikalman proton" (see sec. 4.1.1) are selected. The full final state is reconstructed in the analysis stage. This requires a four-constraint (4C) fit that restricts the sum of the reconstructed four vectors to that of the initial system. Given that the decay tree has been correctly reconstructed, the particles' fitted four-vectors are closer to the generated ones than those that were initially reconstructed. In addition mass cuts are applied for the mesons to reduce background from misidentified particles.

6.1.1. π^0 Production

Monte Carlo data for pion production is generated at the minimum beam momentum of 1.5 GeV/ c , at 3 GeV/ c which corresponds to 2.2 GeV beam kinetic energy of the HADES measurement, at 5.4 GeV/ c which is the maximum proton momentum for the upgraded SIS18 and at the maximum HESR momentum of 15 GeV/ c .

Production via $\Delta^+(1232)$

In proton proton reactions neutral pions are, in particular at low beam momenta, predominantly produced via a $\Delta(1232)$ resonance. The $\Delta^+(1232)$ is part of the $J^P = \frac{3}{2}^+$ baryon decuplet (see sec. 2.2.2). It is a spin excitation of the proton with the same quark content. The $\Delta^+(1232)$ is a broad resonance with a Breit-Wigner full width of $\Gamma \approx 117$ MeV, decaying to a nucleon and a pion with BR = 99.4%, [1]. $\Delta(1232)$ production is described by the one-pion exchange model and is dominated by forward angles, e.g. small momentum transfer. The differential cross section is given by

$$\frac{d\sigma}{dt} = \frac{1}{64\pi} |\mathcal{M}|^2 \frac{1}{4I^2}, \quad I = \sqrt{(p_1 p_2)^2 - M_N^4}. \quad (6.1)$$

t is the standard Mandelstam variable, I a kinematic factor with $p_{1,2}$ the beam and target proton four-vectors and M_N the nucleon mass. The spin averaged matrix element \mathcal{M} is given in [9].

The distribution of the pion's decay angle in the $\Delta(1232)$ rest frame is expected to be of the form $1 + A \cos^2 \theta_\pi^\Delta$, [11].

An illustration of the reaction is given in fig. 6.1. The two initial protons are exchanging a pion which excites one of the protons to a $\Delta^+(1232)$, afterwards decaying into a proton and a π^0 .

Fig. 6.2 shows the generated and reconstructed Dalitz plot for the resonant π^0 production data set at $p_{\text{beam}} = 3$ GeV/ c . There are some entries outside of the allowed phase space in the reconstructed Dalitz plot. They correspond to a few misidentified events. The bands at $m_{p\pi^0}^2 = m_\Delta^2 = 1.52$ GeV corresponding to the $\Delta^+(1232)$ resonance are clearly visible. Although the reconstruction efficiency for this reaction is quite small, the generated Dalitz plot is reproduced very well. The full phase-space is covered in the reconstruction, showing the advantage of a 4π -detector. The position and shape of the resonance shows good agreement with the Dalitz plot in [3] measured by HADES.

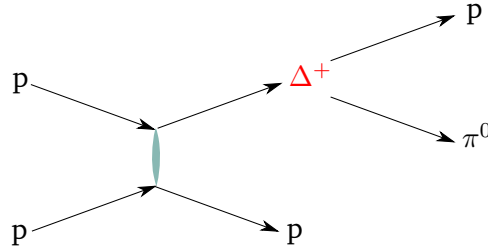


Figure 6.1.: Illustration of the production of a π^0 through a Δ^+ resonance in pp scattering.

6.1.2. η Production

The minimum center of mass energy that is required to produce an η in pp scattering is

$$\sqrt{s} = 2m_p c^2 + m_\eta c^2 = 2.45 \text{ GeV} \quad (6.2)$$

and corresponds to a beam momentum of $1.983 \text{ GeV}/c$. Simulated beam momenta in the η case are $2.056 \text{ GeV}/c$ to test production just above threshold, and $3 \text{ GeV}/c$, $5.4 \text{ GeV}/c$ and $15 \text{ GeV}/c$ as in the π^0 case. Resonant production at the η threshold is not possible since the formation of a resonance requires additional energy. The minimum center of mass energy for resonant production is

$$\sqrt{s} = m_p c^2 + m_{N^*} c^2 = 2.47 \text{ GeV}. \quad (6.3)$$

This is just above the η production threshold. The lowest beam momentum is omitted in the resonant scenario.

Production via $N^+(1535)$

The lightest baryon that is decaying into an η meson with a significant branching ratio is the $N^+(1535)$. It is also the baryonic resonance through which η production is happening to a large fraction [3]. The $N^+(1535)$ has spin-parity $J^P = \frac{1}{2}^-$ and a Breit-Wigner mass $m \approx 1530 \text{ MeV}$ and full width $\Gamma \approx 150 \text{ MeV}$. It is dominantly decaying into a nucleon and a pion with $\text{BR} = 35 - 55 \%$ and into a nucleon and an eta meson with $\text{BR} = 32 - 52 \%$. An illustration of the reaction is given in fig. 6.3. The two initial protons are exchanging a pion which transforms one of the protons into an $N^+(1535)$, afterwards decaying into a proton and an η .

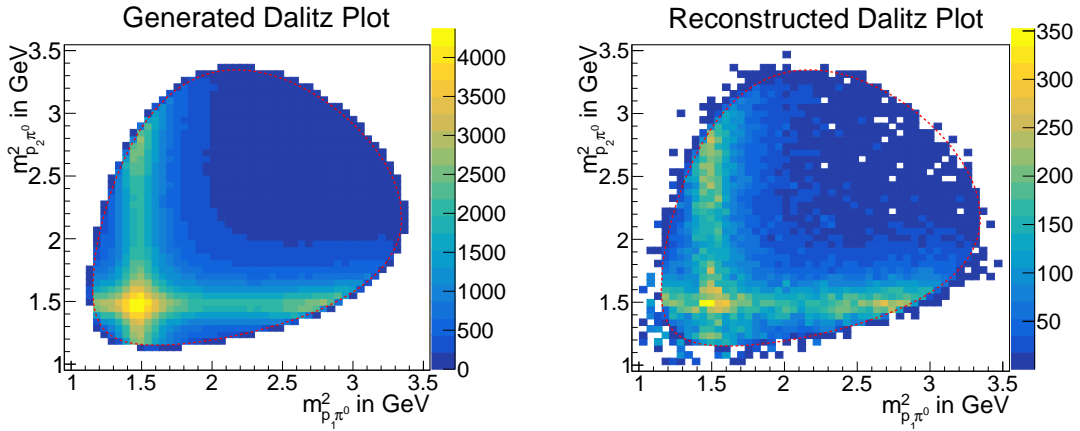


Figure 6.2.: Dalitz plot for the $pp\pi^0$ final state at $\sqrt{s} = 2.77$ GeV. The Delta resonance is easily identifiable. In the reconstructed Dalitz plot the selection criterion $\chi^2_{4C} < 200$ is chosen for event selection and the π^0 mass is fitted using (5.1) to calculate the yield for each bin. The information from the 4C-fitted four-vectors is used for bin assignment. The red dotted line indicates the phase-space boundary.

The generated and reconstructed Dalitz Plot for the resonant η production data set at $p_{\text{beam}} = 5.4$ GeV/ c is shown in fig. 6.4. The bands at $m^2_{p\eta} = m^2_N = 2.36$ GeV just at the lower edge of the phase space are corresponding to the $N^+(1535)$ resonance. The generated Dalitz plot is reasonably reconstructed. The full phase-space is covered as well for this reaction channel. The blue dots outside of the phase space border are single misidentified events and represent significantly less events than the blue area inside the allowed phase space. The position and shape of the resonance shows good agreement with the Dalitz plot in [19] measured by HADES.

6.2. Reconstruction Performance

6.2.1. Event Selection

For event selection a cut on the χ^2 of the 4C fit is applied and a signal function with a second order polynomial background is fitted to the peak corresponding to the relevant

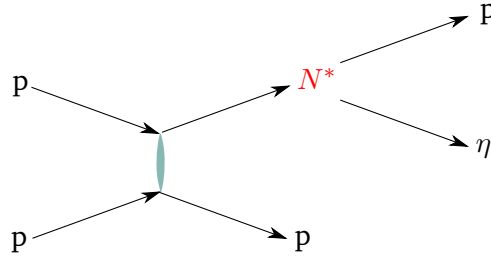


Figure 6.3.: Illustration of η production through a N^+ resonance in pp scattering.

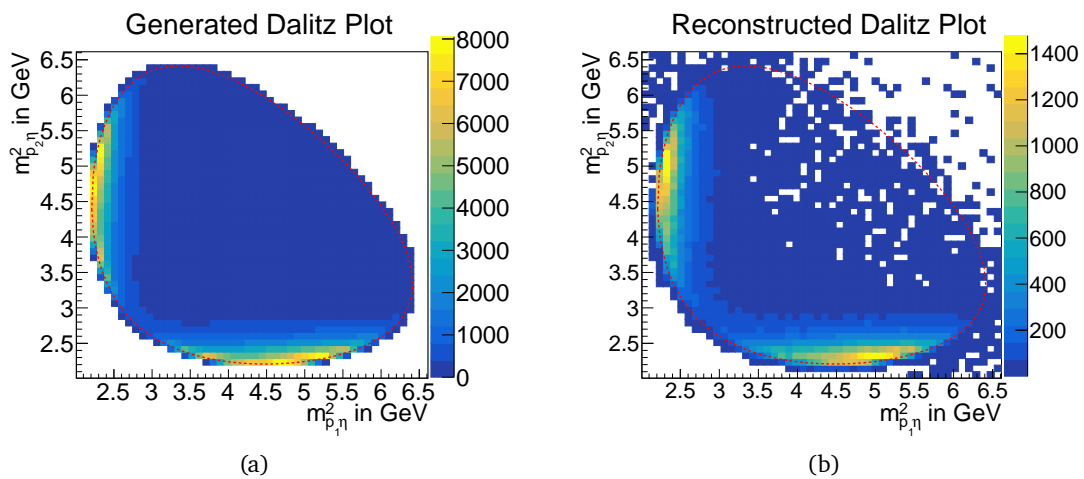


Figure 6.4.: Dalitz plot for the $pp\eta$ final state at $\sqrt{s} = 3.47$ GeV. The Delta resonance is clearly visible. In the reconstructed Dalitz plot the selection criterion $\chi_{4C}^2 < 100$ is chosen for event selection and the η mass is fitted using (6.4) to calculate the yield for each bin. The information from the 4C-fitted four-vectors is used for bin assignment. The red dotted line indicates the phase-space boundary.

Table 6.1.: Contribution of different error sources to the total uncertainty.

Error contribution in %	statistic	χ^2 cut of 4C fit	mass fit
π^0	6.1	61.7	75.1
η	13.5	75.6	25.1

meson in the invariant mass spectrum of its daughter photons. The total yield for the respective channel is determined by calculating the integral of the signal function. This can be done for the initially reconstructed spectrum as well as for that after the 4C fit has been applied. Since the so obtained yield might depend on the choice of the χ^2 cut ($\chi^2 < 50, 100$ and 200 are tested here) and whether the unfitted or fitted invariant mass spectrum is used, different combinations of those possibilities are used to estimate the systematic uncertainty of the result. Function (5.1) is chosen to determine the yield of the signal for the unfitted invariant mass spectrum and for the fitted invariant mass spectrum a double-gaussian as in (6.4) is selected.

$$f(x) = A \cdot \exp \left[-\frac{1}{2} \left(\frac{x - \mu}{\sigma_A} \right)^2 \right] + B \cdot \exp \left[-\frac{1}{2} \left(\frac{x - \mu}{\sigma_B} \right)^2 \right] \quad (6.4)$$

A and B are the magnitude parameters and σ_A and σ_B the widths of the two gaussians. μ is the common mean.

Tab. 6.1 lists the different contributions to the total error of the efficiency. It has been shown that the statistical error on the total efficiency is small when employing Monte Carlo data sets of this size. In case differential cross sections are studied, more Monte Carlo data might be necessary to determine the respective efficiencies precisely. The largest fraction of the systematic error of the π^0 reconstruction efficiency is produced by the different yields obtained whether the fitted or unfitted invariant mass spectrum is used. This effect is less dominant regarding the η reconstruction efficiency. The choice of the χ^2 cut of the 4C fit has a larger impact here. This uncertainty could be removed by choosing the same cuts for real and generated data.

Invariant mass spectra, showing the π^0 and η peak respectively for phase space distributed data at $p_{\text{beam}} = 5.4 \text{ GeV}$, are shown in fig 6.5 representatively.

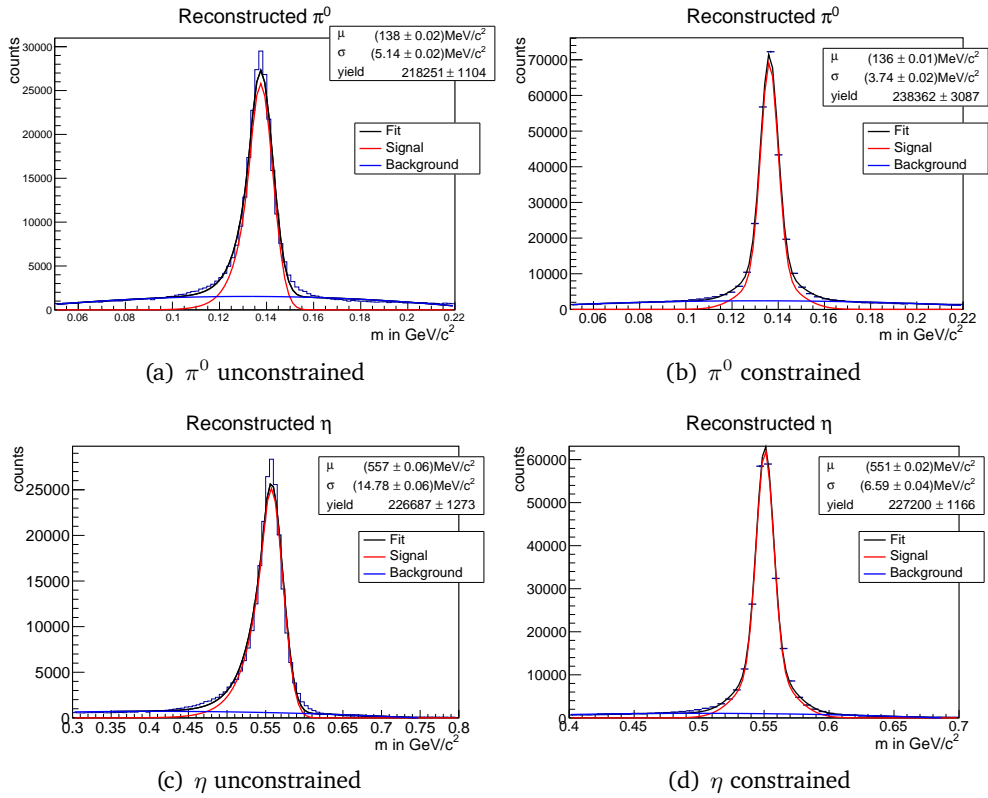


Figure 6.5.: Example invariant mass spectra of π^0 and η , with and without adjustment from the 4C fit. $p_{\text{beam}} = 5.4 \text{ GeV}$, non-resonant generation and $\chi^2 < 100$.

6.2.2. Efficiencies

The efficiencies obtained by this procedure are shown in fig. 6.6 for the different center of mass energies and for resonant and phase-space distributed meson production. The efficiency is rather low at low energies ($\approx 10\%$). This is probably due to the low proton momenta where acceptance is low. If the π^0 is produced via a $\Delta^+(1232)$ resonance, the reconstruction efficiency gets even lower when energy is increasing. Fig. 6.7 shows the $p - \vartheta$ distributions of the generated protons at the highest available center of mass energy for both scenarios. Because the Δ is produced mainly at low momentum transfer, the beam proton keeps most of its forward boost and goes into the very forward direction, where there is no acceptance and gets lost in most cases. Thus, combining the very slow target proton with the forward going beam proton leads to a very low efficiency. In the phase-space distributed scenario the protons are mainly generated with medium momentum and polar angle which makes them more likely to be reconstructed. In reality the Δ resonance is only dominant at $\sqrt{s} < 3.3$ GeV [3] and the angular distribution of the protons might look different for other resonances. Considering the non-resonant data sets the reconstruction efficiency is equally good for the π^0 and η samples. It stays at about the same level at about 20 % to 25 %, as soon as the protons have enough energy to emerge the beam pipe. This is in agreement with the individual reconstruction efficiencies of protons and the mesons. In case of resonant η production, the reconstruction efficiency is even slightly enhanced at low center of mass energies compared to the phase-space distributed case. The reaction products are going dominantly into regions where good detection is provided as shown in fig. 6.8. Nevertheless there is an efficiency drop at the highest beam momentum since the relative momentum transfer is smaller here. The meson direction is of less importance to the total efficiency since there are no significant acceptance holes except the missing EMC slices which reduces the reconstruction performance for all scenarios.

6.3. Cross Sections

Since the measurement of cross sections requires data by its nature, only the error of cross sections in PANDA measurements can be estimated using simulations. The cross section of some particular reaction can be written as

$$\sigma = \frac{N}{t \cdot l \cdot \epsilon} \quad (6.5)$$

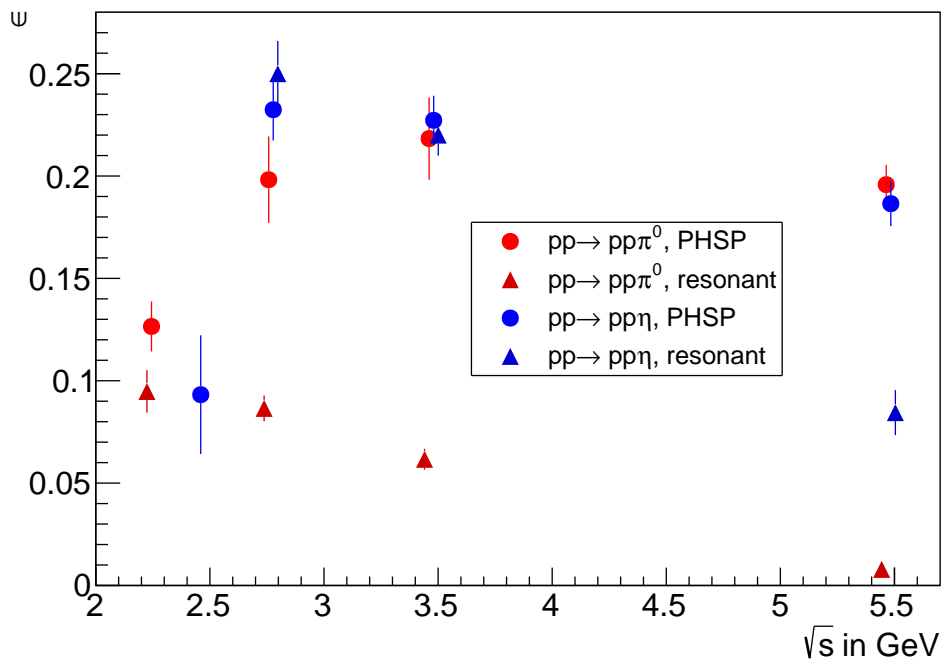


Figure 6.6.: Calculated efficiency for the reconstruction of the complete final state of $pp \rightarrow pp\pi^0$ (red points) and $pp \rightarrow pp\eta$ (blue points) in the resonant and phase-space distributed scenario at different center of mass energies.

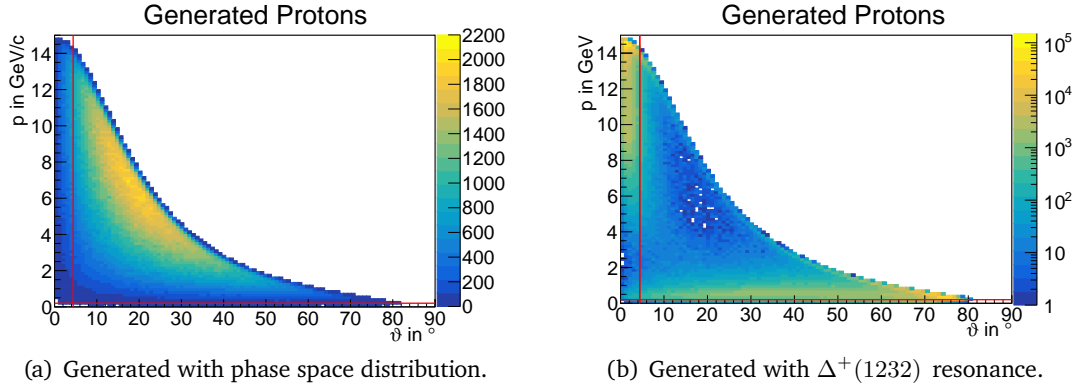


Figure 6.7.: $p - \vartheta$ distributions of the generated protons in the resonant and phase space distributed π^0 production scenario at $p_{\text{beam}} = 15$ GeV. The red lines at $p = 0.2$ GeV and $\vartheta = 4.4^\circ$ indicate the lower bounds of the reconstructable phase space for protons (see sec. 5.4).

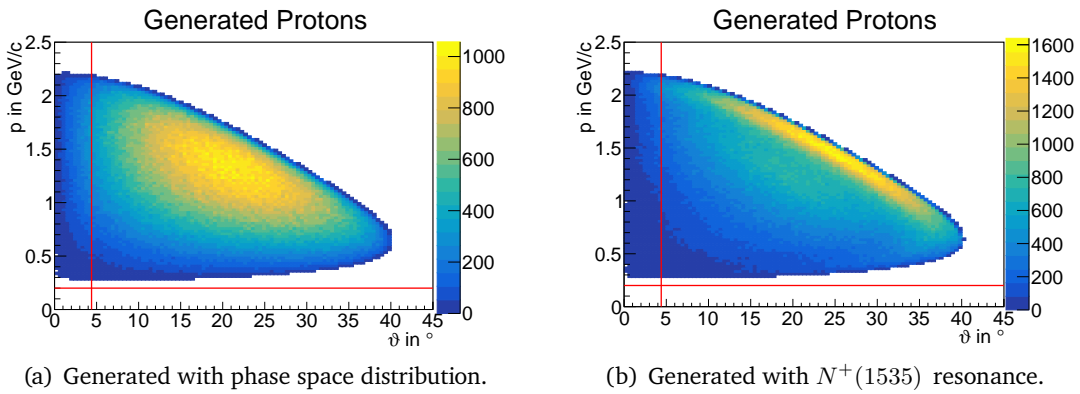


Figure 6.8.: $p - \vartheta$ distributions of the generated protons in the resonant and phase space distributed η production scenario at $p_{\text{beam}} = 3$ GeV. The red lines at $p = 0.2$ GeV and $\vartheta = 4.4^\circ$ indicate the lower bounds of the reconstructable phase space for protons (see sec. 5.4).

where N is the number of reactions being reconstructed in data, t the measuring time and l the luminosity. In case not the total cross section is measured but only one specific decay of a reaction product (e.g. only the $\gamma\gamma$ decay of the η), the cross section has to be corrected with the corresponding branching ratio BR

$$\sigma = \frac{N}{t \cdot l \cdot \epsilon \cdot \text{BR}}. \quad (6.6)$$

It is assumed that t and l are fixed but the other variables are error-prone. N has a statistical error of \sqrt{N} , the uncertainty of ϵ was estimated in the last section and ΔBR is given in the data tables in [1]. The total uncertainty of the cross section is

$$\Delta\sigma^2 = \left(\frac{\partial\sigma}{\partial N}\Delta N\right)^2 + \left(\frac{\partial\sigma}{\partial e}\Delta e\right)^2 + \left(\frac{\partial\sigma}{\partial \text{BR}}\Delta \text{BR}\right)^2 \quad (6.7)$$

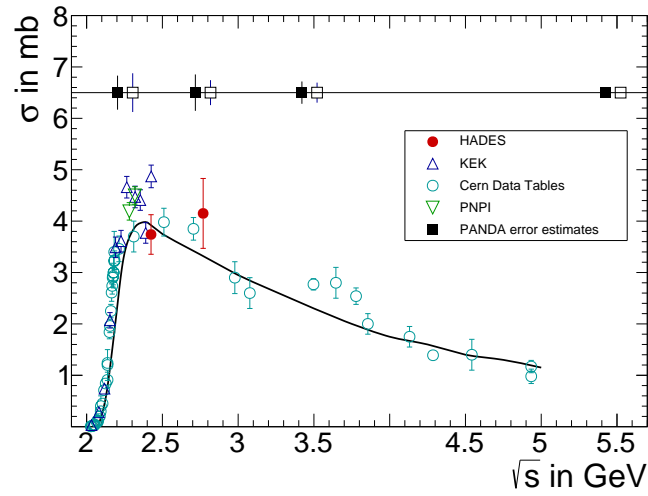
$$= \left(\frac{1}{\text{BR} \cdot t \cdot l \cdot e} \sqrt{N}\right)^2 + \left(\frac{N}{\text{BR} \cdot t \cdot l \cdot e^2} \Delta e\right)^2 + \left(\frac{\text{BR}}{\text{BR}^2 \cdot t \cdot l \cdot e} \Delta \text{BR}\right)^2 \quad (6.8)$$

$$= \left(\frac{\sigma}{\text{BR} \cdot t \cdot l \cdot e}\right)^2 + \left(\frac{\sigma}{e} \Delta e\right)^2 + \left(\frac{\sigma}{\text{BR}} \Delta \text{BR}\right)^2. \quad (6.9)$$

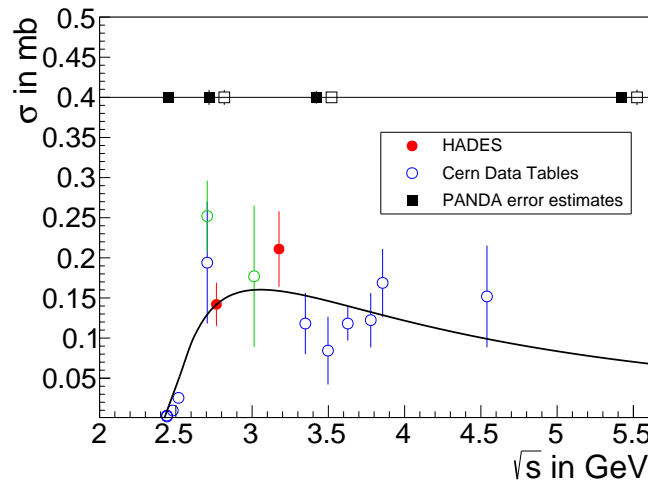
Fig. 6.9 shows a model prediction [20] and existing experimental data [3, 19] for the energy dependent total cross section for π^0 and η production in pp scattering. The error estimates of a PANDA measurement are shown as well for comparison. The cross section predicted by the model is used to calculate the error. Furthermore a luminosity of $l = 10^{30} \text{ s}^{-1} \text{ cm}^{-2}$ and a measuring time of 10 min is assumed. The error is dominated by the uncertainty of the efficiency.

The error bars are of about the same size in the resonant and non-resonant scenario. In case of π^0 production it is visible that the error bars at small energies where the cross section is large, are larger than those at higher energies and smaller cross section. The ratio $\Delta\sigma/\sigma$ stays rather constant over the probed energy range. Overall the estimated error bars are comparable with the ones from existing data and it is expected that measurements at high center of mass energies with PANDA will have a good precision.

In the η case there exists much less data from other experiments. Due to the smaller uncertainty of the reconstruction efficiency for $pp \rightarrow pp\eta$ a very good performance is expected here. The estimated error bars are significantly smaller than those of existing measurements.



(a) $pp \rightarrow pp\pi^0$



(b) $pp \rightarrow pp\eta$

Figure 6.9.: Energy dependent total meson production cross sections, adapted from [3]. The solid curve displays the total resonance model cross section from [20], the colored dots measurements from other experiments. The estimated error for a $\bar{\text{P}}\text{ANDA}$ measurement in the phase space (full squares) and resonant (open squares) scenario are shown at the top.

7. Conclusions

The performance of the $\bar{\text{P}}\text{ANDA}$ day-1 detector setup to measure π^0 and η production cross sections in proton scattering has been studied. As a first basic step the detector acceptance and reconstruction efficiency of the relevant particles has been determined in chapter 5.

It has been shown that the averaged reconstruction efficiency for single photons is 85 % and 90 % for the forward endcap and barrel EMC respectively. The resolution is better than 2 % for photons above 1 GeV and meets the requirements stated in the TDR. The forward Shashlyk EMC has to be included properly in PandaRoot to get reasonable results for photon reconstruction in the very forward direction at high energy.

The π^0 reconstruction efficiency is about 70 % in directions where there is an active EMC detector which is in agreement with the photon efficiency. π^0 detection is very sensitive to the detector structure due to the relatively small opening angle of the daughter photons. When averaging over the full solid angle, the reconstruction efficiency is about 40 %. Merged π^0 (i.e. the opening angle of the photons is so small that just one cluster is produced) are not expected to occur when a proton beam is used.

The reconstruction efficiency for η is similar to the π^0 efficiency but less dependent on the detector structure because of the larger opening angle of the daughter photons and independent of the η momentum. The missing slices of the barrel EMC reduce the reconstruction performance for neutral particles but not the phase space coverage of the detector due to its symmetry in φ .

In addition the detector acceptance for protons has been probed. It is around 80 % for most of the solid angle. There is little acceptance in the very forward direction and no acceptance at $\vartheta < 4.4^\circ$ which might be a result of two missing forward tracking stations in the day-1 setup, leading to too few hits for track reconstruction.

Given the information from the single particle studies the performance of $\bar{\text{P}}\text{ANDA}$ to reconstruct the full final state of meson production reactions in pp scattering has been tested in chapter 6. Therefore different scenarios for resonant and non-resonant π^0 and

η production have been simulated. It has been shown that it is possible to reconstruct the full Dalitz plot, i.e. there are no significant acceptance holes in the phase space. The reconstruction efficiencies for the full final state have been determined and their uncertainties estimated. Comparing the different scenarios it has been revealed that the reconstruction efficiency is very much dependent on the scenario, especially on the respective scattered proton directions. Therefore it is important to choose the right scenario/resonance contribution if reconstruction efficiencies for data correction are to be determined. Theoretical predictions, information from existing data or a partial wave analysis could be applied here. The full phase space coverage makes the conduction of the latter possible.

Since the cross section of π^0 and η production is quite large in pp scattering and due to the high luminosity, a reasonable amount of events can be taken in less than one hour. These studies are an excellent choice for the early stages of \bar{P} ANDA. The energy range of the HESR fits perfectly and the very good coverage of the detector makes precise measurements of total as well as differential meson production cross sections possible which will be an improvement to existing data taken at low energy or with unprecise bubble chamber experiments. This data might give new insights in the production mechanisms of baryonic resonances as well as estimates nucleon nucleon cross sections which are crucial to understand heavy ion collisions

A. Reconstruction of Merged π^0

One possibility to reconstruct "merged π^0 , i.e. π^0 whose daughter photons produced a cluster in the EMC that cannot be split by the usual bump-splitting algorithm, is to calculate the invariant mass of that cluster based on the moment analysis of clusters. The procedure presented here is adapted from [8]. It provides correct results assuming the transversal shape of a photon shower is energy independent and symmetrical. Experimental effects like the incidence angle or passive material derade the performance of the method.

The procedure requires the calculation of the energy-weighted moments

$$\langle x^n \rangle = \frac{\sum E_i x_i^n}{\sum E_i} \quad (\text{A.1})$$

of the cluster up to the third order. The sum is looping over all EMC digis contributing to the cluster. x_i are their center coordinates and E_i the respective deposited energy. In order to simplify the calculation, the transversal frame (x_0, y_0) is rotated into the $\langle x_0 y_0 \rangle$ co-moment eigengram (x, y) as shown in fig. A.1. The $\langle xy \rangle$ co-moment vanishes by definition in this frame and the new x-axis is the cluster's major axis. Due to the assumed symmetry of the shower, the unknown positions of the photon hits (x_A and x_B) should lie on that axis. The rotation angle ϕ with respect to the original frame is given by

$$\tan 2\phi = \frac{2 \langle x_0 y_0 \rangle}{\langle x_0^2 \rangle - \langle y_0^2 \rangle}. \quad (\text{A.2})$$

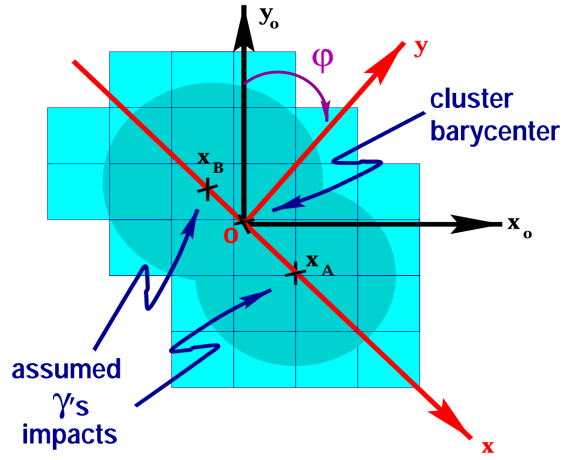


Figure A.1.: Rotation of the transversal frame (x_o, y_o) into the co-moment eigenframe (x, y) . The cluster barycenter lies in the origin of both frames and the positions of the photon impacts lie on the x -axis of the rotated frame.

In addition the following relations occur in the (x, y) eigenframe:

$$\begin{aligned}
 E &= E_a + E_b && \text{cluster energy} \\
 \langle x^1 \rangle &= \frac{x_A E_A + x_B E_B}{E} = 0 && \text{1st moment (barycenter) set to the origin} \\
 \langle x^2 \rangle &= \frac{x_A^2 E_A + x_B^2 E_B}{E} + \sigma_x^2 && \text{2nd moment (variance)} \\
 \langle x^3 \rangle &= \frac{x_A^3 E_A + x_B^3 E_B}{E} + \sigma_x^2 && \text{3rd moment (skewness)} \\
 \text{with } \sigma_x^2 = \sigma_y^2 = \langle y^2 \rangle &&& \text{because of shape symmetry}
 \end{aligned}$$

This system of equations can be solved to obtain solutions for the four unknowns x_A , x_B , E_A and E_B . Assuming the two impact points' separation is small with respect to the distance to the primary vertex, the invariant mass can be written as

$$M_{AB}^2 = \frac{E^2}{r^2} (\langle x^2 \rangle - \langle y^2 \rangle). \quad (\text{A.3})$$

where d is the distance between the primary vertex to the cluster. This result can be expressed in the original frame that is π -rotated with respect to the co-moment eigenframe:

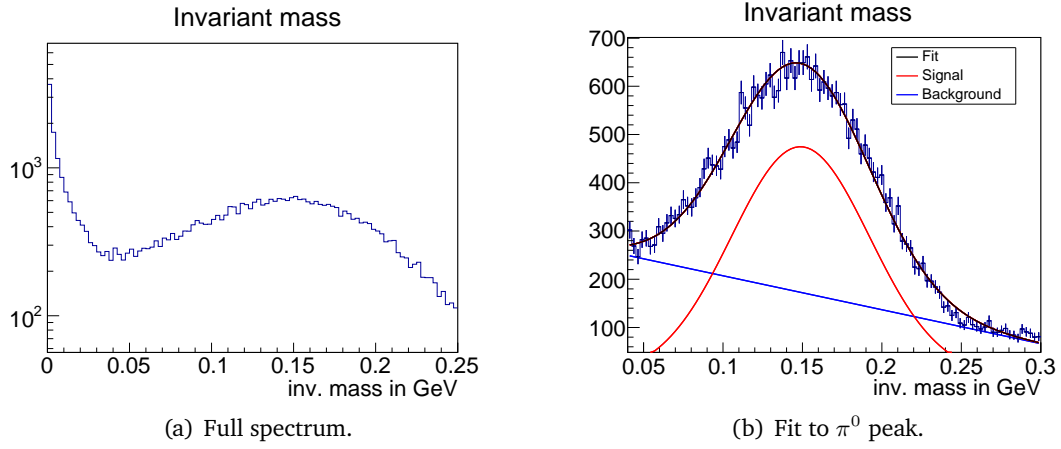


Figure A.2.: Single cluster invariant mass spectrum calculated by the moments analysis of clusters. The large amount of clusters with m_{inv} close to 0 are produced by single photons, those at about m_{π^0} to merged π^0 .

$$M_{AB}^2 = \frac{E^2 \langle x_0^2 \rangle - \langle y_0^2 \rangle}{r^2 \cos 2\phi} \quad (\text{A.4})$$

In order to test the procedure described above, a test π^0 sample consisting of 100000 π^0 generated in the barrel EMC region ($22^\circ < \vartheta < 140^\circ$) at $p_{\pi^0} = 15$ GeV is produced using the box generator. This is an unphysically large momentum but assures that many of the π^0 are merged. After reconstruction the invariant mass of each cluster is calculated according to (A.4). The resulting spectrum is plotted in A.2. The large amount of clusters with a very low invariant mass corresponds to clusters that are produced by one single photon. The other peak in the spectrum at about the π^0 mass corresponds to clusters from merged π^0 . A gaussian with a linear background function is fitted the π^0 peak. The obtained π^0 yield is $\approx 19\,500$ and $\sigma = ?$. It shows that the procedure is working. The π^0 peak is quite broad but separated from the photon peak which makes it possible to identify π^0 candidates that would be lost otherwise.

Bibliography

- [1] Tanabashi et al. “Review of Particle Physics”. In: *Phys. Rev. D* 98 (3 Aug. 2018), p. 030001. DOI: 10.1103/PhysRevD.98.030001. URL: <https://link.aps.org/doi/10.1103/PhysRevD.98.030001>.
- [2] Sylvie Braibant, Giorgio Giacomelli, and Maurizio Spurio. *Particles and Fundamental Interactions : An Introduction to Particle Physics*. 2012. URL: <https://doi.org/10.1007/978-94-007-2464-8>.
- [3] HADES Collaboration. “Study of exclusive one-pion and one-eta production using hadron and dielectron channels in pp reactions at kinetic beam energies of 1.25 GeV and 2.2 GeV with HADES”. In: *The European Physical Journal A* 48.5 (May 2012), p. 74. ISSN: 1434-601X. DOI: 10.1140/epja/i2012-12074-9. URL: <https://doi.org/10.1140/epja/i2012-12074-9>.
- [4] PANDA Collaboration. *Technical Design Report for PANDA Electromagnetic Calorimeter (EMC)*. 2008. eprint: arXiv:0810.1216.
- [5] PANDA Collaboration. *Technical Design Report for the Panda Forward Spectrometer Calorimeter*. 2017. eprint: arXiv:1704.02713.
- [6] PANDA Collaboration. *Technical Design Report for the: PANDA Micro Vertex Detector*. 2012. arXiv: 1207.6581 [physics.ins-det].
- [7] PANDA collaboration. *Technical Design Report for the Panda Forward Tracker*. 2018.
- [8] O Deschamps et al. *Photon and neutral pion reconstruction*. Tech. rep. LHCb-2003-091. Geneva: CERN, Sept. 2003. URL: <https://cds.cern.ch/record/691634>.
- [9] V. Dmitriev, O. Sushkov, and C. Gaarde. “ π -formation in the $1\text{H}(3\text{He}, 3\text{H})\pi^{++}$ reaction at intermediate energies”. In: *Nuclear Physics A* 459.3 (1986), pp. 503–524. ISSN: 0375-9474. DOI: [https://doi.org/10.1016/0375-9474\(86\)90158-2](https://doi.org/10.1016/0375-9474(86)90158-2). URL: <http://www.sciencedirect.com/science/article/pii/0375947486901582>.

-
- [10] W. Erni et al. “Technical design report for the \bar{P} ANDA (AntiProton Annihilations at Darmstadt) Straw Tube Tracker”. In: *The European Physical Journal A* 49.2 (Feb. 2013). ISSN: 1434-601X. DOI: 10.1140/epja/i2013-13025-8. URL: <http://dx.doi.org/10.1140/epja/i2013-13025-8>.
- [11] I. Fröhlich et al. “Pluto: A Monte Carlo Simulation Tool for Hadronic Physics”. In: *PoS ACAT* (2007), p. 076. DOI: 10.22323/1.050.0076. arXiv: 0708.2382 [nucl-ex].
- [12] David J. Griffiths. *Introduction to elementary particles*. 2004. URL: <http://dx.doi.org/10.1002/9783527618460>.
- [13] Yorikiyo Nagashima. *Elementary particle physics : 2. Foundations of the standard model*. 2013. URL: <http://dx.doi.org/10.1002/9783527648887>.
- [14] *PANDA Website*.
- [15] K. Peters. *PANDA Annual Report 2018*. Annual Report. GSI.
- [16] Stefano Spataro. “The PandaRoot framework for simulation, reconstruction and analysis”. In: *J. Phys. Conf. Ser.* 331 (2011), p. 032031. DOI: 10.1088/1742-6596/331/3/032031.
- [17] P. Spiller and G. Franchetti. “The FAIR accelerator project at GSI”. In: *Nuclear Instruments and Methods in Physics Research Section A: Accelerators, Spectrometers, Detectors and Associated Equipment* 561.2 (2006). Proceedings of the Workshop on High Intensity Beam Dynamics, pp. 305–309. ISSN: 0168-9002. DOI: <https://doi.org/10.1016/j.nima.2006.01.043>. URL: <http://www.sciencedirect.com/science/article/pii/S0168900206000507>.
- [18] *Infographics gallery | CERN*.
- [19] KHALED and TEILAB. “ π^+ AND π^0 MESON PRODUCTION IN p+p REACTIONS AT $E_{kin} = 3.5$ GeV”. In: *International Journal of Modern Physics A* 26.03n04 (2011), pp. 694–696. DOI: 10.1142/S0217751X11052554. eprint: <https://doi.org/10.1142/S0217751X11052554>. URL: <https://doi.org/10.1142/S0217751X11052554>.
- [20] S. Teis et al. “Pion-production in heavy-ion collisions at SIS energies”. In: *Zeitschrift für Physik A Hadrons and Nuclei* 356.4 (Dec. 1996), pp. 421–435. ISSN: 0939-7922. DOI: 10.1007/bf02769248. URL: <http://dx.doi.org/10.1007/BF02769248>.